Spectroscopy and nuclear dynamics of starburst galaxies

Vermaas, L.

2

The asymmetric nuclear region of M83 and its off-centre starburst

L. Vermaas and P. P. van der Werf
submitted to Astronomy & Astrophysics, 2011

Abstract

M83 is a nearby (D=4.5 Mpc) barred spiral hosting a nuclear starburst. Our near infrared integral field spectroscopic data show the complexity of the inner 330×330 pc. The nuclear region reveals a pronounced asymmetry, with the optical peak displaced eastwards from the centre of fainter isophotes, and the main starburst region displaced westwards. We find that Brγ emission from young star clusters in the starburst region accounts for 70% of the total Brγ emission (the rest of Brγ emission being diffuse). Ages derived for the young star clusters show only a very small spread, suggesting a large-scale instability triggering this episode of star formation approximately simultaneously over 250 pc. In contrast to the Brγ emission, the [FeII] emission, tracing shocks from supernova remnants, is distributed in a large number of small and compact clumps and we show that these each correspond to one or at most a few supernova remnants. In contrast to Brγ, [FeII] is dominated by diffuse emission (74% of the total [FeII] emission), and we show that this diffuse emission also results from strong shocks. H_2 emission is found associated both with SNRs (where H_2 line ratios are found to be thermal) and with star forming regions (where H_2 line ratios indicate UV-pumped fluorescence), but like [FeII], 75% of the total H_2 emission is diffuse in nature. Integrated over the central 330×330 pc, at most 10% of the H_2 $v = 1-0$ S(1) emission appears to be UV-excited.

We also study the velocity and velocity dispersion fields of both the stars and the gas. The stellar velocity dispersion shows no well defined peak and we rule out the presence of a large obscured mass concentration close to the centre of the faint isophotes, which had been suggested previously. The gas velocity field shows part of the molecular ring observed earlier using millimetre interferometry. Our data reveals a sharp inner edge to this ring, where a transition to a velocity field with a different kinematic major axis is seen; this transition may result from the presence of different orbital families in the barred potential. The gas velocity field also shows localised rotation centred on the optical peak, and we use this feature to determine a lower limit to the mass of the optical peak of $2.6 \cdot 10^7 M_{\odot}$. Our data furthermore show that the optical peak, while not currently forming stars, has undergone a recent episode of star formation, as shown by the presence of luminous supernova remnants. We discuss the implications of our results for our understanding of the remarkably asymmetric nuclear region of M83.

2.1 Introduction

The barred spiral galaxy M83 is one of the closest galaxies hosting a nuclear starburst. It is almost face-on (i=24° Comte 1981), and at a distance of 4.5 Mpc (Thim et al. 2003) it allows excellent spatial resolution (1″=22 pc) over the active region. The nuclear region has been studied in detail for many years, but disagreement still exists on the location of the dynamical centre of M83. Cowan et al. (1994) showed that the optical/NIR peak does not coincide with the radio emission peak. A $J-K$ colour image by Elmegreen et al. (1998) revealed two non-concentric rings of enhanced extinction in the nuclear region: an outer ring with a radius of 8.6″ (190 pc), connecting to the two inner spiral arms and centred 2″ south and 1.4″ west of the optical peak, and an inner ring with a radius of 2.8″ (62 pc) and centred on the the optical peak. An arc or partial ring of enhanced star formation (Gallais et al. 1991) is located in the region between these rings. Thatte et al. (2000) report that the centre of the K-band isophotes at radii more than 10″ is offset from the optical peak, and located at approximately the same location as the centre of the outer ring found by Elmegreen et al. (1998). Furthermore, Thatte et al. suggest the existence of a second, obscured nucleus at this position, based on the fact that the stellar velocity dispersion as measured from long-slit spectroscopy of the 2.3 μm displays a second peak there. Finally, Sakamoto et al. (2004) used millimetre interferometry to study the velocity field of CO emission, and found the dynamical centre to be offset from the optical peak, at about the same location as Thatte's "invisible nucleus". Mast et al. (2006) combined optical Hubble Space Telescope data with ground-based integral field spectroscopy in the R-band and suggest the presence of a hidden mass concentration, more massive than the optical peak, at a different position: 4″ northwest of the optical peak and 4″ north from the dynamical nucleus of Sakamoto et al. (2004). Maddox et al. (2006) find several peaks in the radio regime, and confirm the offset of the brightest 20 cm radio peak from the optical peak.

In general, starbursts are associated with interacting or merging galaxies. M83 has a companion galaxy at a distance of 0.5 Mpc, NGC 5253, which hosts a nuclear starburst. However, no clear signature of interaction has been found in M83 itself. Furthermore, the last encounter with NGC 5253 was about 1 Gyr ago, which was too long ago to trigger the present starburst, which is much younger with an estimated age of 6 Myr (Houghton & Thatte 2008). It has been proposed that the capture of a small object by the galaxy has led to formation of the bar and triggered the starburst (e.g., Sakamoto et al. 2004, Díaz et al. 2006). Recent observations of gas kinematics show the gas flow from outer regions to the centre, and indicate that an inner Lindblad resonance can be responsible for the accumulation of gas in the nuclear region, resulting in a starburst (e.g., Fathi et al. 2008). Sakamoto et al. (2004) speculated that the optical peak, which is older than the other nuclear star clusters, could be the remnant of a captured dwarf galaxy. Both Harris et al. (2001) and Houghton & Thatte (2008) studied the ages of the star clusters in the nuclear region and found a clear age gradient, with the youngest clusters in a region west of the optical peak, with older clusters in an arc-like structure extending from this position towards the southeast. Recently, Knapen et al. (2010) confirmed these results and suggested that the offset of the optical peak from the photometric and kinematic centre is the result of an $m=1$ perturbation in the nuclear gravitational potential.

Table 2.1 – Parameters of VLT/SINFONI observations

Night	band	pointings	N_{frames}, t_{int}
2 & 3 April 2005	J, H, K	3 pointings (ABC)	2x300 s/pointing
23 April 2005	H	2 pointings (AB)	2x300 s/pointing
Pointings (field centres)	A (northwest)	B (southwest)	C (optical peak)
RA (J2000)	13:37:00.2	13:37:00.3	13:37:00.8
DEC (J2000)	−29:51:51.6	−29:51:58.6	−29:51:56.6
SINFONI 0.″25 platescale	J	H	K
FOV	$8'' \times 8''$	$8'' \times 8''$	$8'' \times 8''$
spatial pixelscale	$0.''125 \times 0.''250$	$0.''125 \times 0.''250$	$0.''125 \times 0.''250$
wavelength range	1.10 - 1.40 μm	1.45 - 1.85 μm	1.95 - 2.45 μm
spectral resolution $\lambda/\Delta\lambda$	2000	3000	4000

In this paper we present new near-infrared (near-IR) integral field observations of the nuclear region (inner 330×330 pc) of M83. We carry out an analysis of the starburst and its products (star formation rate, cluster ages and masses, supernova rate), and place this in the context of the nuclear dynamics, considering both gas and stars. We specifically investigate the reality of the putative "dark nucleus" using the distribution of stellar velocity dispersions in the nuclear region, and the role of the rotating gas ring detected using millimetre interferometry.

2.2 Observations and data reduction

2.2.1 SINFONI observations

We observed M83 with SINFONI, the Spectrograph for INtegral Field Observations in the Near-Infrared (1.1 - 2.45 μm), which is installed on UT4 (Yepun) of the ESO Very Large Telescope (Eisenhauer et al. 2003, Bonnet et al. 2004). Our observations were carried out in all three atmospheric windows available: the J, H and K bands. The largest platescale was used, with a field of view of $8'' \times 8''$on 64×64 spatial pixels. The spectrum from each pixel is divided over ~ 2000 spectral elements (depending on the band), with spectral resolutions $\lambda/\Delta\lambda$ of 2000, 3000 and 4000 in J, H and K, respectively.

Three overlapping pointings were chosen in the nuclear region. One field was centred on the optical peak, and two pointings west of the nucleus include starburst and continuum peaks that were known from previous observations. Observations in the J, H and K bands were carried out on April 2 and 3 of 2005. Additional H-band observations (without the pointing on the optical peak) were taken on April 23 of 2005. The total integration time for

each pointing was 600 s, split into two observations of 300 s each. Sky frames of the same integration time were taken with each filter for each pair of observations. The K-band seeing during these observations was approximately $0.6''$. Further details are given in Table 2.1.

2.2.2 SINFONI data reduction

The data were reduced with the standard SINFONI pipeline, which was developed by ESO and the Max-Planck-Institut für extraterrestrische Physik. The default procedure included corrections for pixel non-linearity, distortion and wavelength calibration. Flux calibration as well as telluric feature correction was done with observations of a standard star. Each frame was also corrected for spatially variable transmission by applying an illumination correction.

The observations were done in ABA'-nodding mode, i.e. object-sky-object, with the A' frame slightly shifted with respect to the A frame. All observations were carried out with the same setup and the same integration time of 300 s. Thus, for each object frame there is a sky frame observation with the same integration time. However, variability of the sky even on these timescales caused problems, especially in the H-band, which is densest in OH lines. For this reason, in some cases the sky frames were corrected with a multiplication factor of typically a few percent, or a spectral shift up to 0.1 pixel.

A standard star was observed right after each object-sky-object observation at the same airmass. This was typically a B star containing few stellar lines in the NIR. Stars with known J, H and K magnitudes were selected from the Hipparcos catalogue, and were used for telluric feature removal as well as for flux calibration. The standard stars were reduced with the same setup as was used for the science frames. After reduction, the average stellar spectrum was extracted from each standard star frame, and stellar lines were removed (recombination lines, especially the Brackett-series in H-band). The one dimensional spectrum was divided by a blackbody of the same temperature to get a flat spectrum with atmospheric absorption features only. The number of counts was converted to flux using the literature values of the star's magnitude in that band. The spectrum in each pixel of the image was divided by this cleaned standard star spectrum. Telluric absorption features were removed satisfactorily. Flux calibration, however, appeared to be slightly variable between the frames and the observations were calibrated with JHK imaging data obtained with IRAC2 on the ESO/MPG 2.2 m telescope under photometric conditions (see Section 2.2.3).

Finally, for each band, all six datacubes, cleaned, calibrated and illumination corrected, were coadded with the correct shifts to obtain the final mosaic datacube. In every pixel of the SINFONI field of view, ionised and molecular gas spectral emission lines were fitted with single Gaussians. This procedure resulted in images of integrated line flux, velocity and velocity dispersion for the brightest emission lines detected in M83.

2.2.3 IRAC2 data

We established the absolute flux scale of the SINFONI data by comparing to unpublished JHK imaging obtained earlier with IRAC2 (Moorwood et al. 1992) at the ESO/MPG 2.2 m telescope at La Silla, Chile. The camera used a 256×256 HgCdTe array and the $0.27''$/pixel

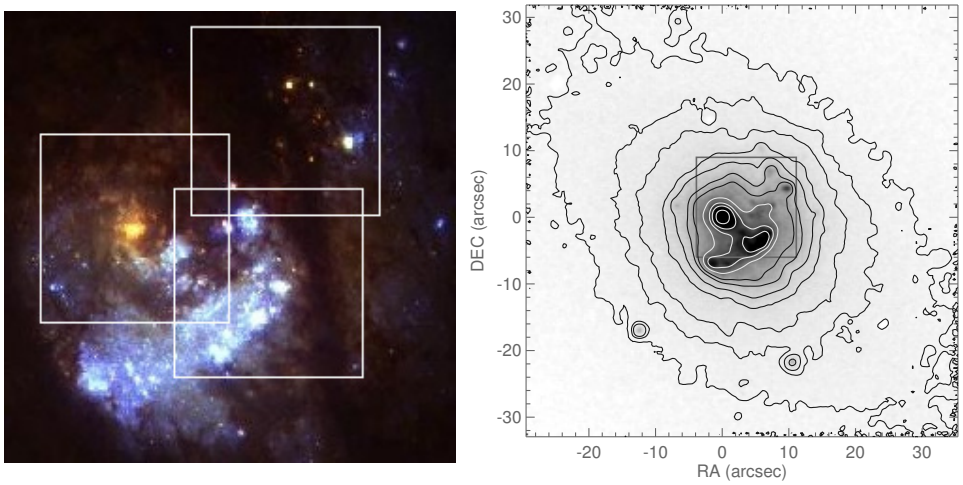

Figure 2.1 – Left: archival HST/WFPC2 image, composite blue (F300W), green (F547M) and red (F814W) filters. The white squares indicate the pointings of the SINFONI observations. Right: IRAC2 *K*-band image with contour overlay (black: [5.0, 7.5, 10, 15, 20, 30, 40]$\cdot 10^{-3}$ erg s^{-1} cm^{-2} μm^{-1}sr^{-1}; white: [60, 80, 100, 150]$\cdot 10^{-3}$ erg s^{-1} cm^{-2} μm^{-1}sr^{-1}); the grey square denotes the outer edges of the combined SINFONI image (as shown in Fig. 2.2).

image scale was employed under photometric conditions on June 17, 1993. Total integration time was 160 s, for *K*-band, 240 s for *H*-band and 320 s for *J*-band, with an equal amount of sky. Photometric calibration was achieved by observations of the F5V star HD 122414 with magnitudes $J = 8.536$, $H = 8.281$ and $K = 8.224$ (Carter & Meadows 1995) at a closely similar airmass. Standard procedures for sky subtraction, flatfielding and interpolation of bad pixels were used. Finally, the frames were aligned and averaged.

2.2.4 VLA data

In our analysis we will also use the radio emission from supernova remnants in M83. Unfortunately, high-quality radio continuum imaging of this region at a resolution comparable to our near-IR data is not available in the literature. We therefore used our own radio continuum imaging obtained earlier with the NRAO Very Large Array. In order to achieve a resolution similar to our near-IR data, we used the hybrid BC configuration (resulting in an approximately circular beam at the Declination of M83) at a frequency of 14.96 GHz. At this frequency, a combination of both thermal bremsstrahlung from HII regions and synchrotron radiation from supernova remnants is expected. The observations used the U-band receiver with a bandwidth of 100 MHz and 2 polarisations in 27 antennas. Total integration time was 5.3 hours, and phase calibration was carried out every 15 minutes. Flux calibration was established using observations of the radio source 3C 286 (assumed flux 538 mJy) before and after the M83 observations. Standard AIPS procedures were used for flagging bad data, amplitude and phase calibration, map making and cleaning. The resulting image has a full width at half

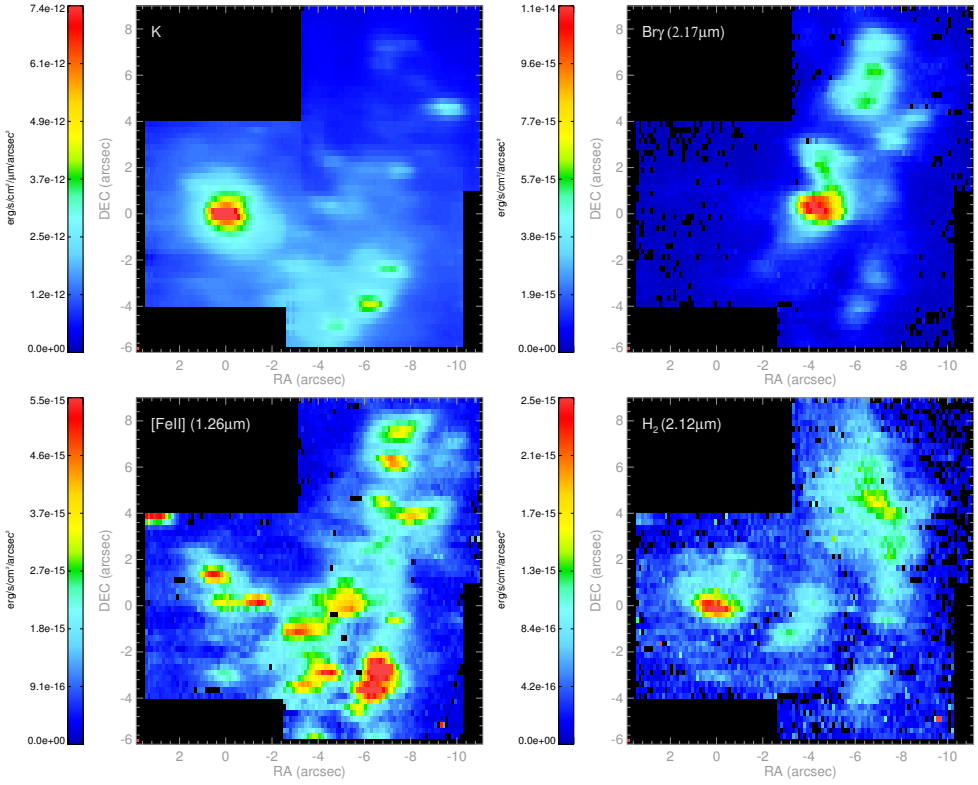

Figure 2.2 – Upper left: K band continuum; upper right: line image of Brγ (2.17 μm); lower left: line image of [FeII] (1.257 μm); lower right: line image of H_2 (2.12 μm). Position (0,0) is in all cases at the peak of the *K*-band continuum.

maximum (FWHM) synthesised beam of $1.23'' \times 1.05''$, at a position angle of 62.2°, and an r.m.s. noise at the field centre of 58 μJy beam^{-1}.

2.3 Results

Our extensive dataset contains a wealth of information on spectral lines (tracing various gas components) as well as stellar emission and absorption features. In order to present these features clearly, we begin with an overview of the region. We then discuss the stellar continuum, followed by the various spectral lines. We then define regions of spectral interest, discussing their integrated spectral properties.

2.3.1 Morphology of the nuclear region of M83

The left frame of Figure 2.1 shows a true-colour image of the nuclear region of M83 in the optical from HST/WFPC2 archival data (2002). The orange peak is the brightest optical/near-

IR feature, and is henceforth referred to as the "optical peak". Its orange colour shows that it is older than the young star clusters in the region that show up in blue/white. The white contours indicate the borders of the SINFONI observations. The composed mosaic image ($15'' \times 15''$, as in Fig. 2.2) corresponds to 330×330 parsec.

2.3.2 Near-IR continuum

The K-band continuum (Fig. 2.2, upper left) is dominated by a strong peak. This peak is resolved with a FWHM of $1\farcs12$ (24 pc). The peak coincides with the brightest optical peak, the orange peak in the HST/WFPC2 composite image, Fig. 2.1 (left). Most of the young blue star clusters seen in the left frame of Fig. 2.1 have counterparts in the near-IR, such as the three peaks lining up in the lower right frame, and the peak in the upper right frame of the SINFONI K-band image.

As a reference, the IRAC2 image in Fig. 2.1 (right) shows the K-band out to a larger scale. Also here the luminous peak is recognised, but it can be seen that it is offset from the centre of the fainter isophotes, as was established already by Thatte et al. (2000). We therefore do not refer to the optical peak as "nucleus", in order to avoid confusion with the isophotal centre or the dynamical centre.

2.3.3 Brγ emission

Brγ (HI 7-4, 2.166 μm, Fig. 2.2, upper right) is, together with Paβ (HI 5-3, 1.281 μm), one of strongest of the hydrogen and helium recombination lines that are visible in the near-IR. These lines originate in HII regions around the hot, young stars that ionise their surrounding interstellar medium and therefore trace recent massive star formation. The line emission peaks in a well defined region that is located $4''$ (~ 90 pc) westward of the optical peak. Although diffuse Brγ emission is detected over the whole observed field, no feature is in particular associated with the optical peak. A second, fainter peak is found in the northwest frame of the mosaic image. Most Brγ features have counterparts in the K-band continuum image, but these are relatively faint.

2.3.4 [FeII] emission

The most prominent iron features are the forbidden emission lines of [FeII] in the J-band at 1.257 μm and in the H-band at 1.644 μm.The distribution of $[\mathrm{FeII}]_{1.26\mu\mathrm{m}}$ is shown in the lower left frame of Fig. 2.2. The line is emitted in peaks that are distributed over the whole field of view. Three of the peaks are associated with the optical peak, while others partly overlap with local peaks of the K-band continuum (southwest) and Brγ (northwest). As will be discussed in Section 2.4.4, these lines trace fast shocks associated with supernova remnants (SNRs), and each [FeII]-peak presumably represents several supernovae. In this scenario the strong shocks associated with the SN-explosion destroy the grains, thereby liberating the iron-atoms that were originally locked up in grains. The iron atoms are then singly ionised, producing the [FeII] lines.

2.3.5 H_2 emission

Warm molecular hydrogen gas is detectable in the near-IR through molecular rotation-vibration lines, of which most are found in the *K*-band. The strongest is the H_2 1-0 S(1) transition line at 2.12 μm, see the lower right frame of Fig. 2.2. The line is mostly concentrated around the optical peak. An arc-shaped structure overlaps with the second peak of Br γ emission, about $6''$ from the optical peak. Some of the excited H_2 (2.12μm)-emission is associated with peaks of [FeII], such as the fainter double peak in the centre of the field and in the lower right, which also lines up with the three peaks in continuum emission. The arc-shape of H_2 (2.12μm) in the western half of the field can recognised in the fainter Br γ-emission as well.

2.3.6 Spectra

Regions of special interest were selected for which spectra were combined. The lines of these spectra were fitted manually with the IDL-based package ISAP. The regions, as indicated by the contours in Fig. 2.3, were defined for pixel values above some threshold of *K*-band continuum (A; white), Br γ (B; red) and $[\mathrm{FeII}]_{1.26\mu\mathrm{m}}$(C; green). The *J*, *H* and *K* spectra of regions A1, B1 and C2 are shown in Figs. 2.4 and 2.5.

Region A1: continuum peak

The top three spectra (top to bottom: *J*-*H*-*K*) in Fig. 2.5 are from region A1, the optical peak region where the near-IR continuum is strong. Several absorption features that arise in the cooler atmospheres of giants/supergiants are detected in *H* and *K*. The most prominent features in our data are the deep ^{12}CO 0-2 at 2.29μm (first overtone), ^{13}CO 1-3 at 2.32μm and ^{13}CO 0-2 at 2.34μm in the *K*-band, and ^{12}CO 3-6 at 1.62μm in *H*, but also a large number of less prominent absorption features are recognisable, e.g., Si I (1.59μm), Mg I (1.71μm), Na I (2.21μm) and Ca I (2.26μm). Some of the strong absorption features in the *H*-band (1.57μm, 1.58μm, 1.66μm), however, are of telluric origin and result from a combination of high airmass and a discrepancy in airmass between the standard star and the observations of this particular frame, leading to imperfect correction in the data.

As expected, the H_2 (2.12μm) line is visible, as well as [FeII] (1.257 μm) although the [FeII] (1.644 μm) hardly stands out because of lower data quality. Also Br γ (2.17 μm) and Pa β (1.28 μm) are clearly recognisable despite the fact that this is only "diffuse" extended emission, not directly associated with the optical peak (see Fig. 2.2).

Region B1: Br γ peak

The three top spectra in Fig. 2.4 are from the strongest Br γ peak, and show the typical spectral lines of bright HII regions. Br γ (2.17 μm) and Pa β (1.28 μm) are very strong, and the Brackett series (Br10-Br19 and further) especially stands out in the *H*-band. Helium recombination lines are visible in all of the *J* (1.28μm), *H* (1.70μm) and *K* (2.06μm) bands. In addition to the HII region lines, lines of OI and [PII] are found in *J*. The OI 1.317μm line is a fluorescent line excited by UV radiation in the neutral gas very close to ionisation fronts

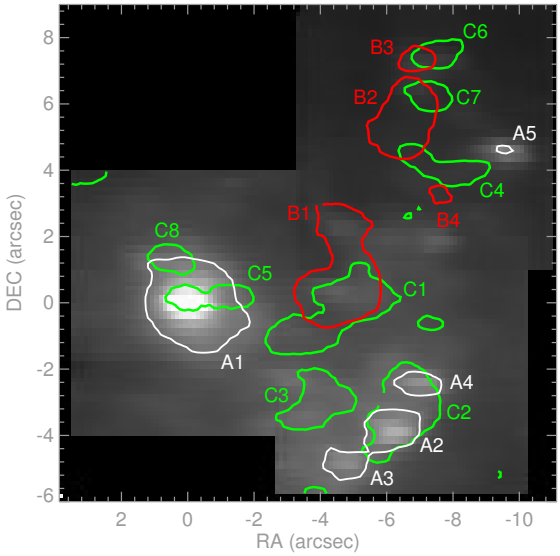

Figure 2.3 – Regions defined by specific thresholds. White (A1-A5): K-continuum $> 2.5 \cdot 10^{-12}$erg s^{-1} cm^{-2} μm^{-1}arcsec^{-2}; red (B1-B4): Brγ (2.17μm)$> 3.8 \cdot 10^{-15}$erg s^{-1} cm^{-2} arcsec^{-2}; green (C1-C8): [FeII] (1.257μm)$> 2.6 \cdot 10^{-15}$erg s^{-1} cm^{-2} arcsec^{-2}. Line fluxes of different regions are given in Table 2.2, spectra of regions A1, B1, B2 and C2 are in Figs. 2.4 and 2.5. The underlying grayscale shows the K-band continuum.

(Walmsley et al. 2000). The [PII] line at 1.188μm traces partially ionised regions irradiated by X-rays from an Active Galactic Nucleus (AGN) or, in the present case, in the hot UV-illuminated layers of Photon-Dominated Regions (PDRs), as argued by Oliva et al. (2001). The Brγ region overlaps with a region of [FeII] (C1) which also shows H_2 emission, and many stronger and weaker emission lines of both are visible in all bands ([FeII] in J and H, H_2 mainly in K). The continuum is about 3 times lower than on the optical peak, but most of the absorption features are visible.

Region C2: [FeII] peak

The three spectra at the bottom of Fig. 2.5 are from a region that has strong [FeII] emission, that peaks between two continuum peaks and is also slightly enhanced in Brγ. [FeII] especially stands out in the H-band spectrum (1.64μm), where the Brackett lines are totally absent, although Brγ and Paβ are moderately strong and even HeI is present at 2.06μm. Weaker lines of [FeII] are not as abundant as may be expected, and may be masked by photospheric features in the strong continuum. The CO absorption bands in K are strong, and also many absorption features are visible in H. It is noteworthy that the [PII] line at 1.188μm, which has very similar excitation requirements to the [FeII] lines, is totally absent. As argued by Oliva et al. (2001), this indicates a strongly enhanced abundance of gas-phase iron, and is direct evidence of grain destruction in fast shocks.

Region B2: second Brγ (and H_2) peak

The bottom three spectra in Fig. 2.4 are from region B2, the second brightest Brγ peak which also coincides with the concentration of H_2 on the arc-like structure (see Fig. 2.2, lower right). The continuum in this region is faint, and the CO-absorption bands in K are shallow, but present. All the Brackett lines and important [FeII] lines are detected, as well as OI and [PII], and in this case also many H_2 lines show up over the whole wavelength range. Besides the first order rotation-vibrational lines of $J = 1-0$ and $2-1$, such as H_2 $1-0$ S(1) at 2.12μm, several higher order lines of the $3-1$ and $2-0$ bands are detected (see Table 2.6).

2.4 Analysis

In this section we will relate the starburst tracers in M83 to underlying physical processes and quantify these in order to understand the temporal and spatial evolution of this circumnuclear starburst. Extinctions are calculated from two different line ratios, star formation properties are derived from recombination lines and cluster ages are modelled with Starburst99 (Leitherer et al. 1999, Vázquez & Leitherer 2005). [FeII] is used as a tracer of supernova activity. Pinning down the origin of the H_2 emission is not trivial, but is enabled by the detection of many lines from many different levels. The morphology of the emission from different species is compared both with the VLA-2cm radio map and mid-infrared PAH emission. The continuum, linestrengths and extinction estimates for the regions as defined in Fig. 2.3, as well as for two background regions, are listed in Table 2.2.

2.4.1 Extinction

Foreground extinction can be calculated using line pairs that have (almost) fixed intrinsic ratios by comparing the observed ratio to the theoretical line ratios, and several lines are available for this purpose. The [FeII] lines in the J and H bands (at 1.257 and 1.644 μm, respectively), originate from the same upper level with an intrinsic ratio of 1.36 (Nussbaumer & Storey 1988). Also Paβ (5−3), Brγ (7−4) and the Brackett-series in the H-band (from upper levels 9 - 22 to 4, have almost fixed intrinsic ratios, adopted here from Hummer & Storey (1987) for a temperature of 10^4 K. The extinction can be calculated from the observed line ratios, using the assumption that the dust is located in an absorbing foreground screen and an the extinction law at near-IR wavelengths of the form $A_\lambda \propto \lambda^{-1.8}$ (Martin & Whittet 1990). Figure 2.6 shows the distribution of visual extinction (A_V), derived from from the Paβ/Brγ and the $[\mathrm{FeII}]_{1.26\mu\mathrm{m}}/[\mathrm{FeII}]_{1.64\mu\mathrm{m}}$ ratios. These distributions are similar in their broad features with values ranging from A_V=1 in low-extinction regions, to 10 and higher in high-extinction peaks. The Paβ/Brγ extinction distribution agrees well with that derived from Hα and Paβ by Houghton & Thatte (2008). A dust lane can be identified in the northwest, roughly from (-4,8) to (-9,0), and is clearest in the Paβ/Brγ extinction image. Nevertheless, some remarkable differences exist between the Paβ/Brγ and [FeII] derived extinction distributions, indicating that the young star formation regions traced in Paβ and Brγ are not located in the same dust complexes as the supernova remnants responsible for the [FeII] emission. Generally, peaks of

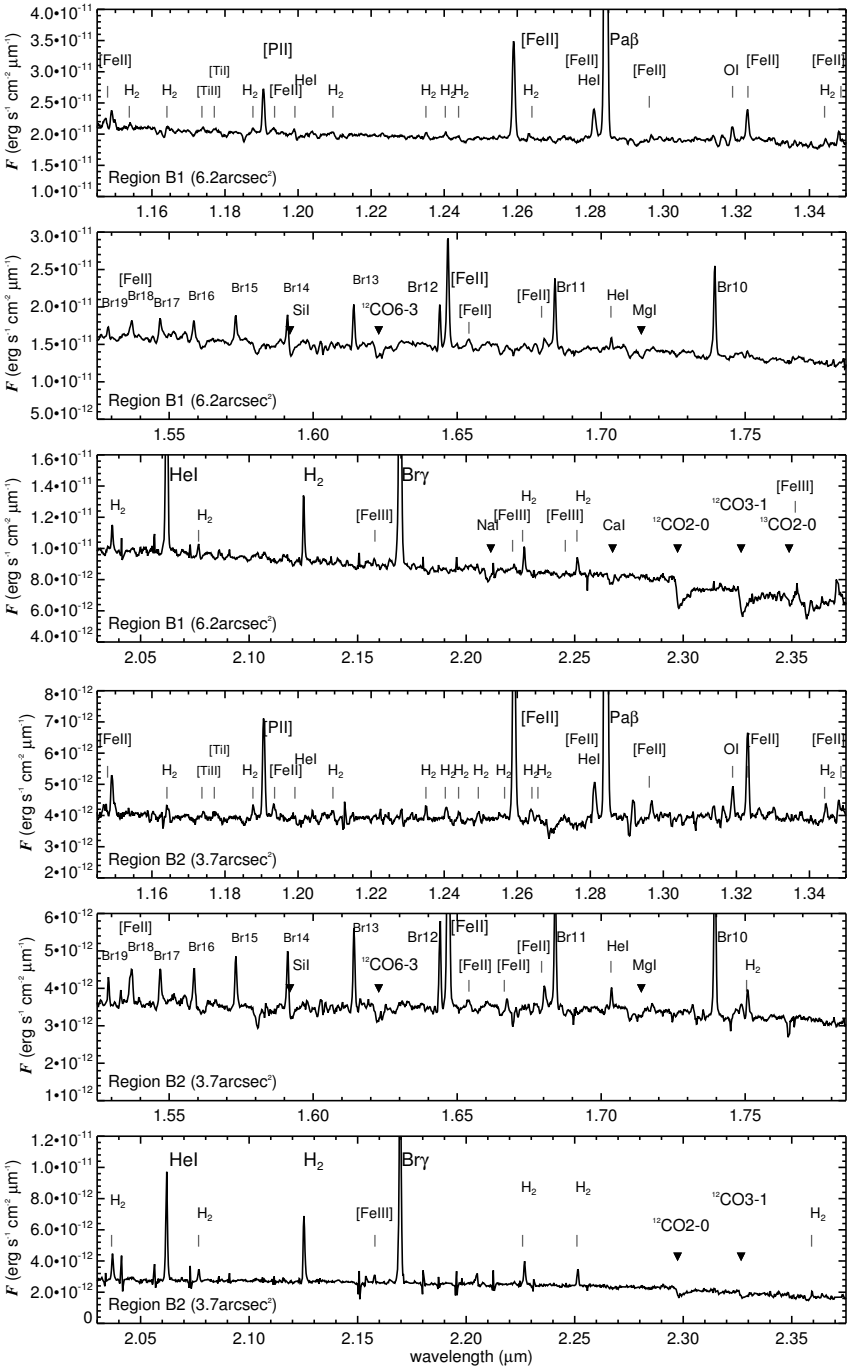

Figure 2.4 – Integrated spectra of Br γ-defined starburst regions B1 (top 3) and B2 (bottom 3) as indicated in Fig. 2.3. Some emission lines are marked with vertical lines, stellar absorption features are marked with filled triangles.

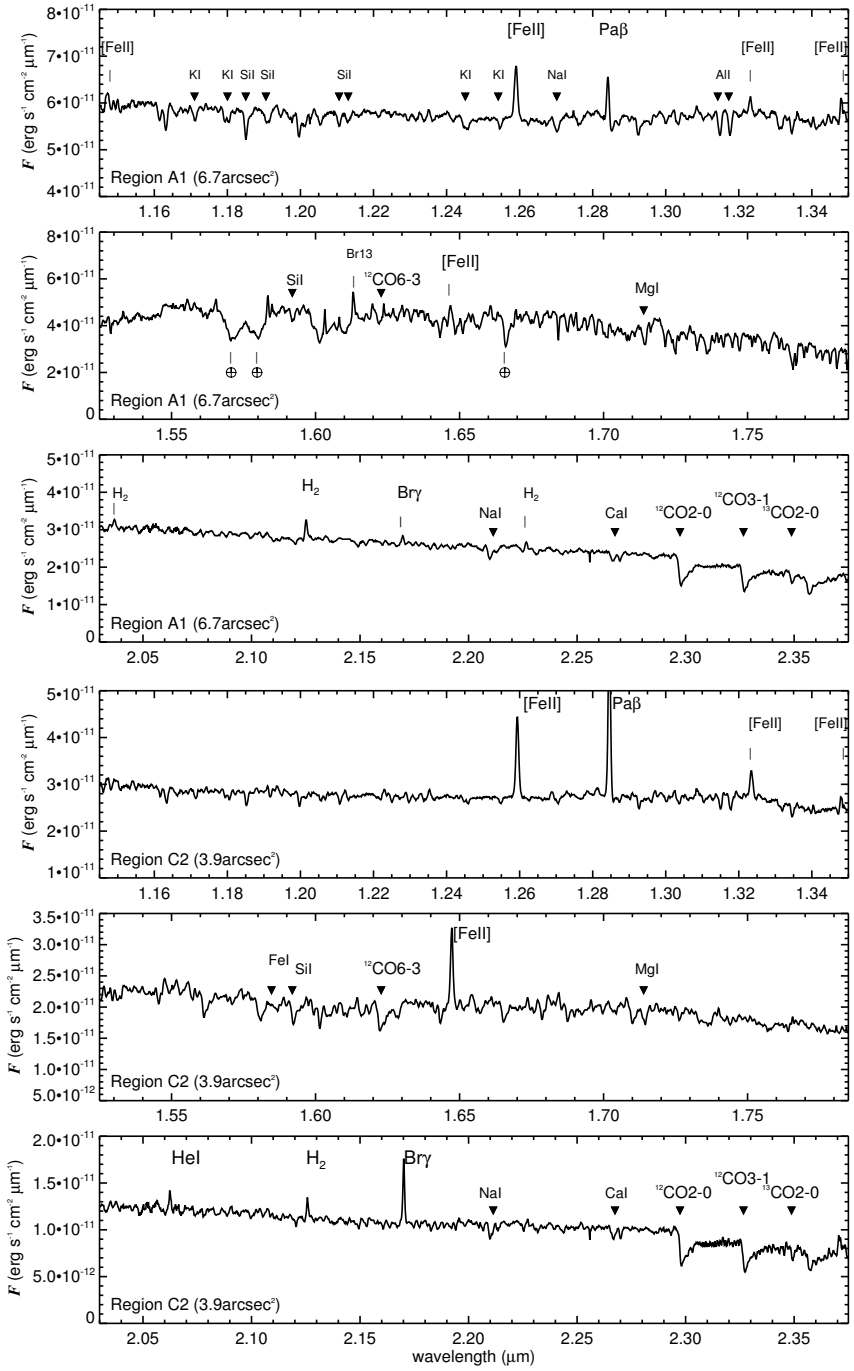

Figure 2.5 – Integrated spectra of regions A1 (top 3, *K*-band continuum-defined), and C2 (bottom 3, $[\mathrm{FeII}]_{1.26\mu\mathrm{m}}$-defined) as indicated in Fig. 2.3. Some emission lines are marked with vertical lines, stellar absorption features are marked with filled triangles, and the earth symbols in the H-band spectrum of region A1 indicate telluric absorption features that could not be removed.

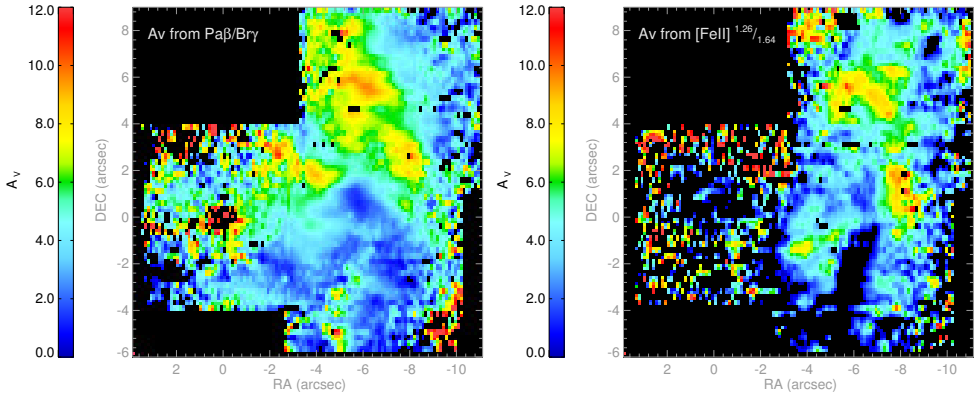

Figure 2.6 – Left: extinction map (A_V) from line ratio Paβ/Brγ; right: extinction map A_V from line ratio $[\mathrm{FeII}]_{1.26\mu\mathrm{m}}/[\mathrm{FeII}]_{1.64\mu\mathrm{m}}$. Note that the poor data quality in H-band in the eastern frame precludes reliable extinction determination from the iron lines in that region. The high extinction on the optical peak (0,0) in the lefthand panel is an artifact resulting from imperfect atmospheric absorption correction in this region.

extinction derived from the Paβ/Brγ correspond to local peaks in the Paβ and Brγ emission, but the most prominent Brγ peak is remarkably extinction-free. In contrast, peaks in the [FeII] derived extinction cannot be readily identified with local peaks in the [FeII] emission. These results suggest that the Paβ/Brγ-derived extinction is more sensitive to dust directly associated with young regions of star formation, while the [FeII] lines trace the more general dust distribution in the starburst region.

2.4.2 Star forming regions

We here refer only to the regions with high Brγ-flux (Fig. 2.3) as (high-mass) star forming regions, although star formation tracers are widespread in the whole field. Extinction-corrected line fluxes and derived properties are in Table 2.3, for the Brγ-defined regions as well as for the *K*-band continuum defined regions.

Ionising radiation field and massive stellar content

The ionisation rate in HII regions is expressed by Q_{Lyc}, the number of photons per second that can ionise hydrogen (Lyman continuum), i.e. photons with energies >13.6 eV. Q_{Lyc} can be estimated from recombination line fluxes, e.g., it relates to Brγ (2.17 μm):

$$Q_{\mathrm{Lyc}} = 1.0 \cdot 10^{51} \left(\frac{F_{\mathrm{Br}\gamma}}{10^{-13}\,\mathrm{erg\,s^{-1}cm^{-2}}} \right) \left(\frac{D}{\mathrm{Mpc}} \right)^2 \mathrm{s}^{-1} \qquad (2.1)$$

where D is the distance and $F_{\mathrm{Br}\gamma}$ is the Brγ flux.

Obviously, stars of a range of spectral types contribute to the ionisation of a single cluster, but it is convenient to follow the approach of Vacca (1994) and translate Q_{Lyc} into the equiv-

Table 2.2 – Integrated continuum and line fluxes and average extinctions of the regions as indicated in Fig. 2.3. The regions with boldface in column (1) have their spectra presented in Figs. 2.4 and 2.5.

Region[d]	Size[a] (pix)	S_K (10^{-13}) $(\mathrm{erg\,s^{-1}cm^{-2}\mu m^{-1}})$	$F_{\mathrm{Br}\gamma}$	$F_{\mathrm{Pa}\beta}$	$F_{\mathrm{HeI(1.70\mu m)}}$	$F_{\mathrm{[FeII]1.26\mu m}}$	$F_{\mathrm{[FeII]1.64\mu m}}$	$F_{\mathrm{H_2\,(2.12\mu m)}}$	A_V	
			$(10^{-16}\,\mathrm{erg\,s^{-1}cm^{-2}})$						(b)	(c)
(1)	(2)	(3)	(4)	(5)	(6)	(7)	(8)	(9)	(10)	(11)
A1	408	252	30	70	-	128	83	10.4	7.5	-
A2	110	54	31	131	12	75	53	10.3	2.7	-
A3	56	25	4.2	13	-	8.3	-	2.6	5.2	-
A4	54	24	16	74	-	36	32	3.2	2.0	2.3
A5	10	4.3	2.0	10	-	2.1	1.7	0.5	1.3	1.2
B1	394	89	392	1340	13	146	140	37	4.5	3.3
B2	226	25	170	408	4.3	72	87	39	7.3	6.2
B3	42	6.5	29	100	0.7	17	19	4.8	4.4	5.3
B4	20	2.8	13	29	0.2	6.3	7.6	3.4	7.9	6.2
C1	300	76	250	954	7.7	156	160	32	3.5	4.2
C2	256	105	75	312	-	178	137	25	2.8	0.57
C3	156	54	25	102	-	85	71	8.4	3.0	1.6
C4	106	15	57	166	-	52	77	19	5.7	8.8
C5	92	78	8.6	22	-	49	62	22	6.8	6.8
C6	60	8.2	32	118	-	28	30	4.5	3.8	4.7
C7	52	6.4	37	108	1.24	29	36	6.9	5.7	6.6
C8	54	21	4.2	16	-	31	20	6.9	3.5	-
bg1[e]	36	6.0	1.4	4.6	-	3.2	2.7	1.2	4.7	1.7
bg2[e]	36	6.3	1.2	5.2	-	3.2	3.3	1.5	2.5	4.2

[a] 1 pixel = $0\farcs125 \times 0\farcs125 = 2.725\,\mathrm{pc} \times 2.725\,\mathrm{pc} = 7.4\,\mathrm{pc}^2$

[b] Extinctions from line ratio $F_{\mathrm{Pa}\beta}/F_{\mathrm{Br}\gamma}$ (intrinsic ratio 5.88), and $A_\lambda \propto \lambda^{-1.8}$ (Martin & Whittet 1990).

[c] Extinctions from line ratio $F_{\mathrm{[FeII]1.26\mu m}}/F_{\mathrm{[FeII]1.64\mu m}}$ (intrinsic ratio 1.36), and $A_\lambda \propto \lambda^{-1.8}$ (Martin & Whittet 1990).

[d] The region numbers correspond to the regions as defined in figure 2.3.

[e] Background measurements from regions of 6×6 pixels with no particular features in the NIR continuum, Br γ, [FeII] or H_2. Regions bg1 and bg2 are centred at (1,-3.5) and (-9,0), respectively.

Table 2.3 – Derived properties of star forming regions. Emission line fluxes and the quantities derived from them have been corrected for extinction using the Paβ/Brγ ratio.

(1)	(2)	(3)	(4)	(5)	(6)	(7)	(8)	(9)	(10)	(11)	(12)
	Size [a]	$F_{\mathrm{Br}\gamma}$ ec	$L_{\mathrm{Br}\gamma}$	$F_{\mathrm{Pa}\beta}$ ec	$L_{\mathrm{Pa}\beta}$	W(CO)	Q [c]	SFR [d]	N_{O7} [e]	$\frac{F_{\mathrm{HeI}(1.70\mu\mathrm{m})}}{F_{\mathrm{Br10}}}$	T (model)
Region	(pix)	$(\mathrm{erg\,s^{-1}cm^{-2}})$	$(L_\odot)$	$(\mathrm{erg\,s^{-1}cm^{-2}})$	$(L_\odot)$	(Å)	$(\mathrm{s^{-1}})$	$(M_\odot\,\mathrm{yr^{-1}})$			(K)
		$\cdot 10^{-16}$	$\cdot 10^{3}$	$\cdot 10^{-16}$	$\cdot 10^{3}$		$\cdot 10^{51}$				$\cdot 10^{4}$
B1	394	555	34.8	3260	205	1.7	11.2	1.1	2240	0.121	3.45
B2	226	300	18.8	1769	111	5.3	6.0	0.6	1200	0.102	3.4
B3	42	41	2.6	239	15.0	6.0	0.83	0.08	166	0.088	3.35
B4	20	24	1.5	142	8.9	12.1	0.49	0.05	98	0.093	3.3
A1	408	54	3.4	318	20.0	13.2	1.1	-	220	-	-
A2	110	38	2.4	225	14.1	14.7	0.77	0.15	154	-	-
A3	56	6.3	0.40	37	2.3	14.4	0.13	0.11	26	-	-
A4	54	19	1.2	110	6.9	11.3	0.38	0.08	76	-	-
A5	10	2.2	0.14	13	0.82	11.9	0.04	0.006	8	-	-
bg1 [f]	36	2.0	0.13	4.7	0.30	13.1	-	0.0004	8	-	-
bg2 [f]	36	1.5	0.09	2.5	0.16	10.2	-	0.0003	6	-	-

[a] 1 pixel = $0\farcs125 \times 0\farcs125 = 2.725\,\mathrm{pc} \times 2.725\,\mathrm{pc} = 7.4\,\mathrm{pc}^2$

[b] Extinctions from line ratio $\mathrm{F}_{\mathrm{Pa}\beta\,1.28\mu\mathrm{m}}/\mathrm{F}_{\mathrm{Br}\gamma 2.17\mu\mathrm{m}}$ (intrinsic ratio 5.88), and $A_\lambda \propto \lambda^{-1.8}$ (Martin & Whittet 1990).

[c] Using equation (2.1).

[d] Calculated by dividing stellar mass formed by age.

[e] Taking $Q_{\mathrm{O7V}} = 5 \cdot 10^{48}\,\mathrm{s^{-1}}$ from Martins et al. (2005).

[f] Background measurements, see Table 2.2 for the definitions of bg1 and bg2.

alent number of O7V-stars for a specific ionised region. Based on Martins et al. 2005), we take $Q_{\rm O7V}$=$5 \cdot 10^{48}\,{\rm s}^{-1}$. Calculated values of Q from $F_{\rm Br\gamma}$ are in column (7) of Table 2.3. The largest and most luminous star formation regions contain a few 1000 (equivalent) O7V-stars (of $\sim 25\,M_{\odot}$), in a region of a few $1000\,{\rm pc}^2$. The smaller regions (few $100\,{\rm pc}^2$) contain a few hundred (equivalent) O7V-stars. Compared to local star forming regions, the large star forming regions are similar to the giant HII region 30 Doradus in the LMC, which contains $\sim 10^4\,M_{\odot}$ in young stars in its central 10 pc core.

Temperature of the radiation field

Photons with energies above 24.6 eV can ionise helium, thus the ratio of He over H recombination lines will give a measure of the hardness of the ionisation field. Although bright, the HeI $(2.06\,\mu{\rm m})$ line is not suitable for this purpose, because the population of the 2^1P state (the upper level of the 2.06μm line) is affected by radiative transfer effects and excitation from the 2^3S state (e.g., Shields 1993, Lancon & Rocca-Volmerange 1996, Lumsden et al. 2001, Rigby & Rieke 2004). Instead, we measured the ratio of HeI $(1.70\,\mu{\rm m})$ over Br 10 $(1.74\,\mu{\rm m})$, which lie close in wavelength and thus are only slightly affected by extinction. With the line ratio, it is possible to model the temperature of the ionisation field (Vanzi et al. 1996, Vanzi & Rieke 1997, Lumsden et al. 2003), which is approximately equivalent to the temperature of the hottest star in the region. This method is only unambiguous for T below $4 \cdot 10^4$ K, where the line ratio saturates (i.e., both the HeI and HI Strömgren spheres are maximally filled). Results for M83 are in Table 2.3, columns (11-12). The radiation field in the brightest Br γ-region (B1) has a temperature of $34.5{\cdot}10^3$ K, which matches an O7 star. The hottest star at the second Br γ-peak (B2) has only a slightly lower temperature of $34{\cdot}10^3$ K matching an O7.5 star. Since in a passively evolving young star cluster the temperature of the radiation field evolves as massive stars move off the main sequence, the HeI/Br10 ratio is also age-sensitive, and we will use this property together with other age indicators in the next section.

Cluster ages and masses

In general, the K-band continuum traces late-type giants/supergiants, the more evolved stellar population. The near-IR luminosity resulting from a single burst comes from red (evolved) stars: first from massive stars that evolved into supergiants (~ 10 Myr), followed by intermediate giants (AGB-stars, $\geq$100 Myr) and finally low mass giants near the tip of the RGB (few Gyr).

In order to determine the ages of the star clusters, we modelled the stellar populations with Starburst99, version 5.0 (Leitherer et al. 1999, Vázquez & Leitherer 2005). A Salpeter IMF (α=2.35) was used with mass cutoff values of $M_{\rm low}$=$0.1\,M_{\odot}$ and $M_{\rm up}$=$100\,M_{\odot}$. We modelled both a single burst (δ-function) up to 15 Myr, and continuous star formation up to 10 Gyr, with metallicities of $Z = 0.020$ ($Z_{\odot}$) and $Z = 0.040$ ($2Z_{\odot}$), the latter matching that of M83 (Zaritsky et al. 1994, Bresolin & Kennicutt 2002). In the continuous star formation model, the Br γ equivalent width starts with a sharp drop from ~ 500 Å to ~ 100 Å between

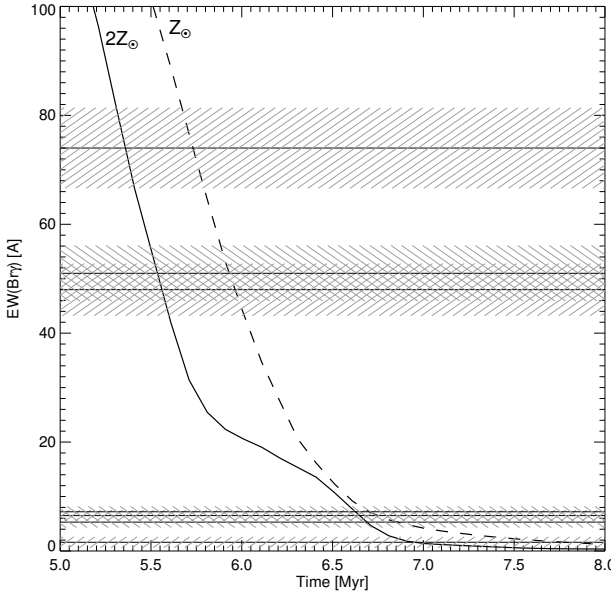

Figure 2.7 – EW(Br γ) modelled with Starburst99 (instantaneous burst, Z=$Z_\odot$ (dashed line) and Z=2$Z_\odot$ (solid line). The horizontal lines represent EW(Br γ) of regions A2-A5 and B1-B4, with the error range shaded. The derived ages are listed in Table 2.4.

8 and 10 Myr, then only slowly declining to ~ 10 Å at 10 Gyr. In this case, the star forming Br γ-defined clusters B1-B4 would have ages of 15 - 60 Myr, but the measured small values of EW(Br γ) of the K-continuum defined clusters A1-A5 (Table 2.4) can never be reached with this mode of star formation. In a single burst model, the HeI-photons disappear at 6.5 Myr, while in the continuous model the HeI/HI ratio rises, to stabilise at some value at 8 Myr. HeI lines are not detected in A1-A5, and in the single burst model these clusters all have ages above 6.5 Myr. For these reasons, we used the instantaneous burst model to determine all the cluster ages.

Ages of the individual clusters were first estimated from the Br γ equivalent widths, which essentially measures ages by comparing the number of OB stars to that of red supergiants. The results are in Table 2.4. No age is given for the optical peak cluster (A1), because there is no sign of recent star formation (Br γ-emission) associated with the cluster and it is clearly older than the rest of the clusters as can be seen from its red colour in the optical HST image in Fig. 2.1 (left). We do derive ages for the other continuum-peaks (A2-A5), since these have enhanced Br γ, and show up as blue (young) clusters in the optical HST image. Cluster masses were then estimated by scaling the model Br γ luminosity of the cluster to the measured $L_{\mathrm{Br}\gamma}$.

Although the Br γ equivalent width method is simple and quantitatively straightforward, it is in practise vulnerable to confusion by K-band (or, less importantly, Br γ) emission unrelated to the cluster under study, in particular when integrating over significant areas. We therefore

also explore two other methods for determining ages. For the Br γ-defined regions, where HeI lines are also detected, the HeI $(1.70\,\mu\mathrm{m})$/Br 10 $(1.74\,\mu\mathrm{m})$ line ratio can also be used to give an age estimate (see Table 2.4). Using two nebular recombination lines has the advantage that the same volume is sampled and minimises the confusion by unrelated diffuse emission. The modelled ages from this line ratio are metallicity dependent and lower than those from EW(Br γ) for solar metallicity, but with twice solar metallicity (as appropriate for M83, see above) they are higher. Given the simplicity of our modelling, the agreement is generally satisfactory. It is however to be noted, that the high HeI $(1.70\,\mu\mathrm{m})$/Br 10 $(1.74\,\mu\mathrm{m})$ ratio of the brightest Br γ source (B1) points to a younger age for this object than for the remaining star forming regions.

Cluster ages can also be derived from the equivalent widths of photospheric CO absorption bands. These bands originate in the cool atmospheres of red giants and supergiants and are sensitive to stellar temperature and luminosity. The CO-index is defined as the ratio between the fluxes integrated over narrow wavelength ranges (width ~ 53 Å), centred on the line and nearby continuum, expressed either in terms of magnitude or as equivalent width. We used the wavelength range definitions of Origlia et al. (1993). CO equivalent widths are stated in column (7) of Table 2.3. The strength of the CO absorption bands is one of the parameters modelled by Starburst99. However, Origlia & Oliva (2000) caution that the CO index is not reliable as an age indicator beyond ~ 10 Myr, because it is observationally difficult to discriminate between strong absorption bands, and weak absorption bands with large widths (i.e., red supergiants and red giants) at these ages. We do see stellar absorption bands in all of our modelled clusters, from which we conclude the presence of stars in an evolved stage (>5.5 Myr). The bands are deeper in the continuum peaks and shallower in the Br γ-defined star forming regions, which qualitatively confirms the relative ages. Again for cluster B1, a very young age of 5.3 to 5.9 Myr (depending on the choice of stellar evolutionary tracks) is indicated by its very low CO equivalent width, in agreement with the young age indicated by the HeI $(1.70\,\mu\mathrm{m})$/Br 10 $(1.74\,\mu\mathrm{m})$ ratio.

Harris et al. (2001) studied 45 star clusters in the central 300 pc of M83 using optical HST data. They found that most of the clusters are in the age-range of 3 - 10 Myr, with the majority of ages between 5 and 7 Myr and the younger clusters located in region B1 in our data. The diffuse background population would be consistent with continuous star formation starting at least 1 Gyr ago. Houghton & Thatte (2008) also modelled the ages of the nuclear clusters of M83. Their single-burst model resulted in conflicting ages as derived from EW(Pa α) and W(CO), with discrepancies of a few Myr. They modelled the star formation history constructing a mixed population model by convolving several single stellar populations (SSPs) from single bursts. Their best fitting model is a sequence of bursts with a duration of 6 Myr and burst-separating times of 0.1 Myr. They again found ages in the range of 5 - 7 Myr, in agreement with Harris et al., but they did not find younger clusters and they ruled out the combination of a SSP contaminated with an old (Gyr) population. They also confirmed the supersolar metallicity. Again their youngest cluster is found in region B1.

The ages derived in this work are also in the range of 5 - 7 Myr, in good agreement with the ages from Harris et al. (2001) and Houghton & Thatte (2008). In this age range, the HeI $(1.70\,\mu\mathrm{m})$/Br 10 $(1.74\,\mu\mathrm{m})$ ratio and W(CO) appear to work remarkably well as age

Table 2.4 – Cluster ages from Brγ and HeI$_{1.70\mu m}$/Br10$_{1.74\mu m}$ ratio modelled with *Starburst99* (instantaneous burst), and derived star formation rates.

Region	EW(Brγ) (Å)	Age (Myr)		M_* ($M_\odot$)	$\frac{\text{HeI}_{1.70\mu m}}{\text{Br10}_{1.74\mu m}}$	Age (Myr)	
		$Z_\odot$	$2Z_\odot$	$\cdot 10^6$		$Z_\odot$	$2Z_\odot$
A1	0.6	-	-	-	-	-	-
A2	6.5	6.8	6.6	1.0	-	-	-
A3	1.6	7.7	7.0	0.8	-	-	-
A4	7.2	6.7	6.6	0.5	-	-	-
A5	5.3	6.9	6.7	0.04	-	-	-
B1	48	6.0	5.6	6.7	0.12	5.5	6.7
B2	74	5.7	5.4	3.5	0.10	5.7	6.8
B3	48	6.0	5.6	0.5	0.09	5.8	6.8
B4	51	5.9	5.5	0.3	0.09	5.8	6.8
bg1	2.9	6.8	7.3	-	-	-	-
bg2	2.3	6.9	7.5	-	-	-	-

indicators, giving consistent results. The fact that the young age of region B1 is not detected when using the Brγ equivalent width as age indicator is likely due to the inclusion of unrelated (foreground or background) K-band emission in the aperture, and cautions against the use of this indicator in crowded regions. Contrary to Houghton & Thatte (2008) we do not find a large discrepancy between ages derived using the various indicators (note that Houghton & Thatte did not have the HeI $(1.70\,\mu\text{m})$/Br 10 $(1.74\,\mu\text{m})$ ratio available), and therefore no need to explore more complex star formation histories for the clusters. The fact that our (idealised) δ-function starburst models are able to represent the observables consistently, using 3 different age indicators, while continuous star formation cannot, can be taken as evidence that the individual bursts occur on timescales significantly shorter than the derived cluster ages.

Star formation in the nuclear region

The star formation rate (SFR) in the nuclear region, averaged over the past 7 Myr (slightly longer than the age of the oldest star forming region) can be estimated by using the masses derived for the star forming clusters (B1-B4 and A2-A5) and dividing by 7 Myr. The resulting nuclear star formation rate in clusters is $1.9\,M_\odot \text{yr}^{-1}$. However, this star formation budget does not account for the significant amount of diffuse Brγ emission, not related to individual clusters. Typical (extinction corrected) flux levels for the diffuse Brγ are given in the "bg1" and "bg2" entries in Table 2.3. Integrated over the observed area, about 30% of the Brγ

emission comes from diffuse regions. This emission may be powered by Lyman continuum radiation leaking out of the bright HII regions, or by unclustered hot stars. In the latter case these stars may be formed in situ, or ejected from young star clusters as proposed by Kroupa & Boily (2002), or result from dissolved young star clusters. In an extensive study of young star clusters in the Antennae (NGC 4038/4039), Mengel et al. (2005) found that clusters dissolve on a timescale of approximately 10 Myr. This result is in agreement with the ages found for the clusters in the present study (all younger than 10 Myr) and the diffuse regions (older than 10 Myr), if we use the high-metallicity models. These results therefore suggest that the diffuse star formation results from clusters that have dissolved in the background field.

Including the contribution from diffuse star formation, the total star formation rate in the region observed here is $2.5\,M_{\odot}\mathrm{yr}^{-1}$ and the average star formation surface density is $3.4\cdot10^{-5}M_{\odot}\mathrm{yr}^{-1}\,\mathrm{pc}^{-2}$. In the brightest star formation region (B1), the star formation surface density is approximately a factor of 10 higher. The average star formation surface density found here is typical for circumnuclear starbursts of moderate luminosity, but significantly lower than that found in the active central regions of Ultraluminous Infrared Galaxies. The average star formation rate surface density found here is larger than that of 30 Doradus in the LMC, which has a star formation rate surface density of 1 - $10\,M_{\odot}\mathrm{yr}^{-1}\,\mathrm{kpc}^{-2}$ over the entire HII-region, and $100\,M_{\odot}\mathrm{yr}^{-1}\,\mathrm{kpc}^{-2}$ in the central 10 pc core.

2.4.3 Comparison with 15 GHz radio emission

The radio emission has both a thermal component from HII regions and a non-thermal contribution from synchrotron radiation. Qualitatively, this can be roughly confirmed by comparing the distribution of 2 cm flux to that of Brγ (HII-regions) and [FeII] from supernova remnants. In Fig. 2.8, from left to right, the 2 cm contours (red) are overlaid on Brγ, H_2 and [FeII] ($1.257\,\mu$m), respectively. The Brγ-peak coincides with the brightest peak of 2 cm emission, while the three small radio peaks in region of the optical/NIR peak (i.e., near the 0,0 position in Fig. 2.8) and the small radio peak in the northeast at the edge of the SINFONI field

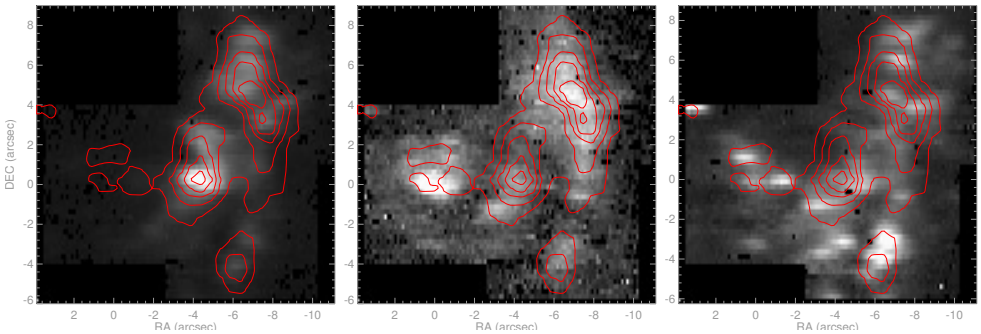

Figure 2.8 – VLA 15 GHz (2cm) radio contours, overlaid on Brγ (left), H_2 (middle) and $[\mathrm{FeII}]_{1.26\mu\mathrm{m}}$(right). Contour levels are [0.25, 0.40, 0.55, 0.70, 0.85] mJy.

are identified with [FeII]-peaks. The main north-south arc of radio emission in the western part of the image closely follows the H_2-arcshape both in morphology and extent. However, this arc partly overlaps with Brγ as well as iron peaks. The thermal and non-thermal components can be separated quantitatively by means of the slope of the emission spectra, as in Turner & Ho (1994) These authors used 6 cm and 2 cm emission maps and assumed a slope of $\alpha = -0.1$ for the flat spectrum component, which they ascribed to thermal bremsstrahlung (free-free) from the brightest HII-regions, and $\alpha = -0.8$ for the steep spectrum component being non-thermal synchrotron emission.

2.4.4 [FeII] emission and supernova activity

Supernova rates in galaxies are usually estimated from the integrated radio continuum emission. The physical background and underlying assumptions are discussed in Condon (1992); see also Condon & Yin (1990), Pérez-Olea & Colina (1995) and Bressan et al. (2002). The observational basis for deriving supernova rates from radio continuum fluxes lies in the infrared-radio correlation, which is remarkably tight and linear (Condon 1992, and references therein), which is attributed to both infrared and radio emission scaling with star formation rate (however, see Bell 2003).

Supernova remnants (SNRs) also radiate strongly in near-IR [FeII] emission lines, with the brightest lines at 1.257 and 1.644 μm (Graham et al. 1987, 1990, Oliva et al. 1989, 1990). Grains in the interstellar medium are destroyed in the shock fronts of the supernova remnants, so that the iron atoms, which are normally mostly locked up in the cores of dust grains, are released into the gas phase and singly ionised by the ambient radiation field. Furthermore, rapid charge exchange with atomic hydrogen converts any Fe^{2+} rapidly into Fe^{+} (Neufeld & Dalgarno 1987), while further neutralisation by charge exchange with atomic hydrogen is prevented since that reaction is endothermic by 5.7 eV.

Based on these results, various authors attempted to use the [FeII] near-IR emission lines for a quantitative supernova rate measurement (Van der Werf et al. 1993, Calzetti 1997, Vanzi & Rieke 1997). The calibration of these relations relies on a comparison of the [FeII] line fluxes with the radio continuum at fixed frequency, and an adopted conversion factor between radio continuum flux and supernova rate (e.g., Huang et al. 1994). However, comparison of high resolution [FeII] line and radio continuum imaging of starburst galaxies indicated that the relation between [FeII] emission and radio emission was complex. Greenhouse et al. (1997) found that there was little direct correspondence between radio-luminous SNRs and peaks of [FeII] emission in M82 and suggested that [FeII] and radio emission select SNRs of different ages. In a high resolution HST imaging study of [FeII] emission of the nearby starburst galaxies M82 and NGC 253, Alonso Herrero et al. (2003) found that only 30-50% of the radio SNRs have a compact [FeII] counterpart, but 70% of the radio flux can be associated with radio SNRs if also diffuse emission is included. Only 22-27% of the [FeII] flux from M82 and NGC 253 is accounted for by discrete sources, so that most of the [FeII] emission from these galaxies is diffuse.

As can be seen in Fig. 2.8, our [FeII] image shows a substantial collection of compact sources, in marked contrast to the emission in Brγ and in H_2, which display larger continuous

Table 2.5 – Properties of the regions defined by [FeII] 1.257μm emission. Emission line fluxes have been corrected for extinction using the $F_{[\mathrm{FeII}]1.26\mu\mathrm{m}}/F_{[\mathrm{FeII}]1.64\mu\mathrm{m}}$ ratio, and derived quantities have been calculated from these extinction-corrected fluxes.

(1) Region	(2) [a] Size (pixels)	(3) [b] $F_{[\mathrm{FeII}]1.26\mu\mathrm{m}}$ ec $(\mathrm{erg\,s^{-1}cm^{-2}})$ $\cdot 10^{-16}$	(4) [c] $L_{[\mathrm{FeII}]1.26\mu\mathrm{m}}$ $(L_\odot)$ $\cdot 10^3$	(5) [b] $F_{[\mathrm{FeII}]1.64\mu\mathrm{m}}$ ec $(\mathrm{erg\,s^{-1}cm^{-2}})$ $\cdot 10^{-16}$	(6) [c] $L_{[\mathrm{FeII}]1.64\mu\mathrm{m}}$ $(L_\odot)$ $\cdot 10^3$
C1	300	372	23.4	273	17.1
C2	256	201	12.6	147	9.2
C3	156	87	5.5	119	7.5
C4	106	323	20.3	238	14.9
C5	92	202	12.7	149	9.4
C6	60	75	4.7	55	3.5
C7	52	114	7.2	84	5.3
C8	54	22	1.4	16	1.0
bg1 [d]	36	4.6	0.29	3.4	0.21
bg2 [d]	36	7.7	0.48	5.7	0.36

[a] 1 pixel = $0\farcs125 \times 0\farcs125$ = 2.725 pc × 2.725 pc = 7.4 pc^2

[b] Extinctions from line ratio $F_{[\mathrm{FeII}]1.26\mu\mathrm{m}}/F_{[\mathrm{FeII}]1.64\mu\mathrm{m}}$ (intrinsic ratio 1.36), and $A_\lambda \propto \lambda^{-1.8}$ (Martin & Whittet 1990).

[c] Assuming D = 4.5 Mpc

[d] Background measurements, see Table 2.2 for the definitions of bg1 and bg2.

regions of emission. The large majority of [FeII] emission features has a counterpart in 15 GHz radio emission and *vice versa*, the only exceptions being the [FeII] emission region at coordinates $(-4,-4)$ and the radio emission region at coordinates $(-4,+2)$ in Fig. 2.8. We draw particular attention to the region around the optical peak (coordinates (0,0)) and northeast from that position, where a very close correspondence is observed between radio and [FeII] emission, while no Brγ emission is observed. The distribution of [FeII] emission in a large number of compact clumps, quite unlike the H_2 and Brγ distributions, suggests that most of these clumps represent remnants of individual supernovae, occurring stochastically in the nuclear region. The presence of 3 such sources in the region of the optical peak, where no active star formation occurs, indicates past star formation activity in this region, and shows directly that supernova activity can persist after active star formation has ceased.

Properties of the [FeII] emission peaks are presented in Table 2.5. After extinction correction, we find total [FeII] 1.64μm luminosities for the individual [FeII] peaks from 1000 to 17100$L_\odot$. While the most luminous and extended [FeII] emission peaks may contain multiple SNRs, the least luminous and most compact regions probably represent individual SNRs, which therefore have typical [FeII] 1.64μm luminosities of a few thousand solar luminosi-

ties. Typical [FeII] 1.64 μm luminosities for optically selected Galactic SNRs are in the range from 0.1 to 6 $L_\odot$ (see the compilation in Morel et al. 2002), but the Galactic SNR RCW 103 is much more luminous with an [FeII] 1.64 μm luminosity of 720 $L_\odot$ (Oliva et al. 1990), and this object provides a fairer comparison, since we are here considering [FeII]-selected SNRs. The well-studied Galactic SNR IC 433 is fainter again with $L(1.257\mu\mathrm{m}) \approx 59\,\mathrm{L}_\odot$ (Keller et al. 1995), implying an [FeII] 1.64 μm luminosity of 43 $L_\odot$. Lumsden & Puxley (1995) observed 8 extragalactic supernovae in M 33, with typical [FeII] 1.26 μm luminosities of 800 $L_\odot$, implying [FeII] 1.64 μm luminosities of 580 $L_\odot$. Labrie & Pritchet (2006) found [FeII] 1.64 μm luminosities of 69 to 780 $L_\odot$ for 17 SNRs in the dwarf irregulars NGC 1569 and NGC 5253. Bright SNRs in the Large Magellanic Cloud have similar [FeII] line luminosities (Oliva et al. 1989). Morel et al. (2002) find [FeII] 1.64 μm fluxes from 6 to 695 $L_\odot$ for a sample of 42 optically selected SNRs in M33.

With [FeII] 1.64 μm luminosities of more than 1000 $L_\odot$, the [FeII] peaks found in the present data are approximately a factor of 10 more luminous than individual SNRs in the Milky Way and nearby galaxies, but comparable to the [FeII] peaks in the nearby starburst galaxy NGC 253, which have typical 1.64 μm line luminosities of $2.6 \cdot 10^3\,L_\odot$ (Forbes et al. 1993). As shown by Morel et al. (2002), the [FeII] luminosity of a radiative SNR depends on the electron density of the post-shock gas, according to the empirical relation

$$\frac{L_{[\mathrm{FeII}]\ 1.64\,\mu\mathrm{m}}}{L_\odot} = 1.1 \frac{n_e}{\mathrm{cm}^{-3}}. \tag{2.2}$$

This expression indicates that for a post-shock density of a few 1000 cm^{-3}, the [FeII] peaks detected in the present data are plausibly accounted for by single SNRs (with the possible exception of the most luminous and extended objects). The density of the post-shock gas can in principle be determined from the ratio of fainter [FeII] lines (Oliva et al. 1990), but none of the density-sensitive lines are detected in our data. However, the detection of thermally excited H_2 emission associated with the SNRs shows that densities of a few times 1000 cm^{-3} are readily achieved in the vicinity of the SNRs (see Sect. 2.4.5).

In our data, we also find significant diffuse [FeII] emission, accounting for 74% of the total [FeII] emission detected, and the [FeII] peaks C1-C8 indicated in Table 2.5 account for only 26% of the total emission. These proportions are quite similar to those found in M82 and NGC 253 (Alonso Herrero et al. 2003). What is the origin of this diffuse emission? In addition to strong shocks destroying the dust grains and single ionising the released iron atoms, [FeII] emission can also originate from partly ionised gas close to the ionisation fronts of HII regions (e.g., Walmsley et al. 2000, Takami et al. 2002) or in X-ray irradiated gas (e.g., Blietz et al. 1994, Mouri et al. 2000). As noted in Sect. 2.3.6, in partly ionised gas the [FeII] emission should be accompanied by [PII] line emission at 1.188 μm, and the absence of the [PII] line (as in our [FeII] peak regions, see Sect. 2.3.6) indicates that the [FeII] emission results from grain destruction in strong shocks. We have inspected our data for [PII] emission in regions of diffuse [FeII] emission (and not associated with recent star formation as revealed by Br γ), and find no detectable [PII] 1.188 μm emission in these regions, while the [FeII] 1.26 μm flux is quite high. This result directly demonstrates that also the diffuse [FeII] emission results from grain destruction in strong shocks. The diffuse emission likely results

from evolved SNRs which have lost their individual identity in but not yet cooled to general ISM temperatures. The highly shearing velocity field, as well as turbulence generated by mechanical energy injection into the ISM by the starburst, may cause the SNRs to dissolve into the ambient ISM more rapidly than in quiescent regions (such as in spiral arms or in the Milky Way), on timescales shorter than the cooling timescale of the post-shock gas.

What do these results imply for estimation of supernova rates from [FeII] line emission? It is clear that the relation between individual radio and [FeII] sources in starburst galaxies is not a simple one. Furthermore, while we have shown that the diffuse [FeII] emission also has a supernova origin, just like the diffuse non-thermal radio emission (e.g., Condon 1992), the range of luminosities and individual SNRs is very large and environment-dependent (see Eq. 2.2). While [FeII] and radio emission both correlate with supernova rate, there is with our present level of understanding no reason to expect a tight and linear relation between integrated [FeII] line fluxes of entire galaxies and their radio continuum fluxes. Indeed, while a relation between [FeII] and radio continuum fluxes for starburst galaxies exists (Forbes & Ward 1993), this relation is not linear and does not go through zero. We can only conclude that the derivation of supernova rates from [FeII] emission fluxes lies on weak grounds and should be avoided until a better understanding of the underlying physics and a proper calibration can be achieved.

2.4.5 H_2 emission

Several rovibrational H_2 lines are detected in our data and listed in Table 2.6. Low order ($v = 1-0$ and $2-1$) lines are present almost everywhere, peaking at the optical peak (region A1) and in the arc-shape that is also recognised in 2 cm radio emission (Fig. 2.8), whereas the higher order lines are exclusively present in the arc-peak (region B2), the location that coincides with the youngest star forming region (Table 2.4). Excitation mechanisms to populate the upper levels of these lines, which lie thousands of K above the ground state, are thermal excitation in shocks (e.g., supernova explosions, stellar winds, cloud collisions), or UV-photons from young OB-stars. Both of these processes can occur in star forming regions, but they populate the energy levels in different ways. In shocks, levels are populated by collisional excitation. The post-shock temperature is typically a few 1000 K, which will populate only the low energy levels (Draine et al. 1983, Hollenbach & McKee 1989, Flower & Pineau Des Forêts 2010). UV-photons have energies high enough to excite the H_2 molecules to higher electronic states, populating also the higher levels when cascading down by fluorescence (Black & Dalgarno 1976, Black & Van Dishoeck 1987). However, at high densities collisions will thermalise the lower levels even if the H_2 emission is fluorescently excited (Sternberg & Dalgarno 1989). In this case the resulting level population is characterised by thermal excitation for the lowest energy levels while higher energy levels are populated by fluorescence and thus show population levels far exceeding those expected for thermal excitation.

The H_2 line fluxes, upper level energies for the star forming region B2 are shown in Table 2.6. This table also gives N/g, the derived upper level column density N divided by the statistical weight g of the level, where the H_2 ortho/para ratio of 3 has been taken into account

Table 2.6 – H_2 emission lines from the star forming region B2. E_{up} denotes the upper level energy of the transition, and N/g is the derived column density N divided by the statistical weight g of the level.

transition H_2	λ (μm)	E_{up}/k (K) $\cdot 10^3$	Flux $(\mathrm{erg\,cm^{-2}})$ $\cdot 10^{-16}$	N/g $(\mathrm{cm^{-2}})$ $\cdot 10^3$
3-1 S(3)	1.1857	19.1	11.9	0.410
3-1 S(1)	1.2330	17.8	9.60	0.629
3-1 S(0)	1.2621	17.4	13.6	6.800
2-1 S(3)	2.0735	13.9	77.8	5.360
2-1 S(2)	2.1542	13.2	6.92	1.872
2-1 S(1)	2.2477	12.5	15.4	2.095
2-0 S(1)	1.1622	12.5	14.3	2.340
2-0 Q(1)	1.2383	11.8	13.6	6.100
2-0 Q(2)	1.2419	12.1	7.03	7.990
2-0 Q(3)	1.2473	12.5	7.14	2.080
2-0 Q(4)	1.2545	13.2	3.98	2.810
1-0 S(7)	1.7480	12.8	13.1	0.852
1-0 S(6)	1.7879	11.5	5.58	1.049
1-0 S(3)	1.9576	8.36	44.1	3.933
1-0 S(2)	2.0338	7.58	21.3	7.647
1-0 S(1)	2.1218	6.95	65.9	12.140
1-0 S(0)	2.2233	6.47	22.5	25.060
1-0 Q(1)	2.4066	6.15	73.0*	28.790

in the calculation of g. The resulting values are shown in the Boltzmann diagram presented in Fig. 2.9.

The column densities of the five lowest $v = 1-0$ lines with upper level energies up to ~ 8000 K show a linear relation with E_{up}, and are therefore thermalised, and can be fit by a Boltzmann distribution with a corresponding excitation temperature of 1080 K. The population of the higher levels is dominated by UV-pumped fluorescence.

In contrast, at the optical peak, where no recent star formation is found, but supernova shocks are revealed in [FeII] emission, only the lowest H_2 lines are found, and with no indication for UV-excitation.

These results directly show that UV-pumping and shock excitation both occur in this starburst nucleus, and they can only be separated by the high spatial resolution of our data, which can associate particular H_2 line emission regions with either supernova shocks (traced by [FeII]) providing thermal excitation of star forming regions (traced by Brγ), providing

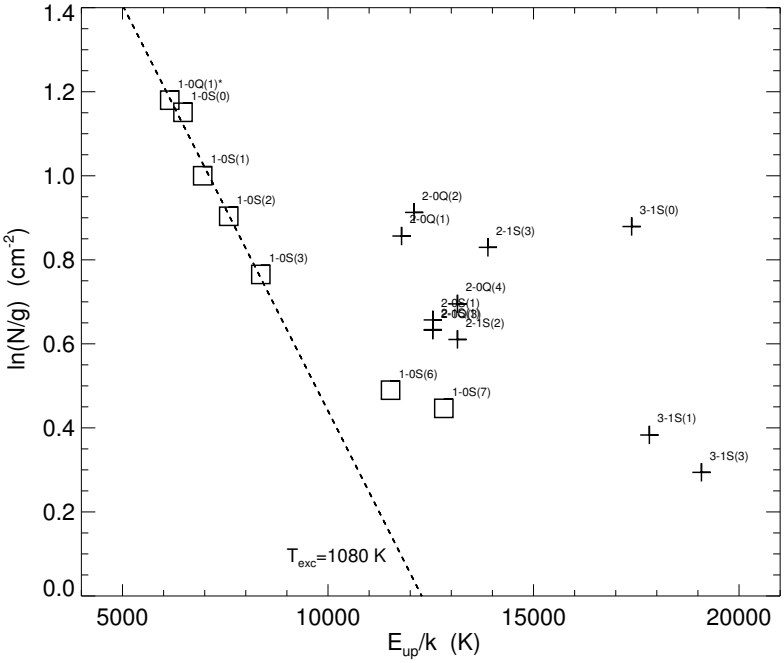

Figure 2.9 – H_2 excitation diagram for the star forming region B2. The data points are normalised to the column density of 1-0 S(1). The dotted line corresponds to the Boltzmann distribution best fitting the five lowest $v = 1-0$ lines, with an excitation temperature of 1080 K. The $v = 1-0$ lines are indicated by squares, higher lines with + signs. $E_{\rm up}$ and N/g are as in Table 2.6.

UV-pumping. Without this spatially resolved information, separation of these two excitation mechanisms would be impossible. Summing the H_2 line fluxes in the star forming regions (B1-B4) and the shocked regions (C1-C8) in Table 2.2 shows that about two thirds of the H_2 emission results from shocks, and only one third is UV-pumped. However, approximately 75% of the total H_2 is diffuse. The diffuse emission may be either UV-excited by photons leaking out of HII regions or by widespread B stars, or shock-excited like the diffuse [FeII] emission. Pak et al. (2004) have argued that in the nearby starburst nuclei in M82 and NGC 253 and the central regions of IC 342 and NGC 6946, UV excitation is the dominant excitation mechanism when integrating over the central kpc (i.e., a region somewhat larger than considered here). In our dataset, the faintness of the H_2 $v = 2-11$ S(1) 2.25 μm line argues against this mechanism, since in the diffuse regions the gas is probably not sufficiently dense to thermalise the upper level of this transition. Our results would then argue for a dominant contribution of shock-excited H_2, with at most 10% of the total H_2 $v = 1-0$ S(1) emission resulting from fluorescence.

2.5 Kinematics

2.5.1 Gas velocity field

Velocity fields were created for all emission lines from the shifts of the (Gaussian) fitted line centres. The velocity resolution corresponding to the instrumental dispersion is 150, 100 and 75 km/s in J, H and K respectively (see Table 2.1). Line centres are fitted with an accuracy of the order of $5 \cdot 10^{-5}\,\mu$m, or ~ 6 km/s. Figure 2.11 shows the velocity and velocity dispersion of H_2 (top left, right) and Brγ (middle left, right). The velocity and velocity dispersion fields of Paβ and [FeII] are very similar to that of Brγ and are therefore not shown. The velocity field of H_2 deviates from the other velocity fields in the region southwest of the optical peak, and this feature will be discussed below (Sect. 2.5.4). The Brγ velocity dispersion (Fig. 2.11, middle right) displays a peak at $(-9,6)$ and a ridge from $(-3,-4)$ to $(-6,3)$. Both features can also be recognised in H_2 (top right), but are less clear because of low signal. On the other hand, the H_2 velocity dispersion shows a peak ($\sim$75 km/s) at the optical peak (0,0), which is not recognised in the other gas velocity dispersion maps.

2.5.2 Stellar velocity field

Due to their intrinsic sharpness, the stellar CO photospheric absorption bands at 2.3 μm offer an excellent feature for probing the stellar kinematics. We have used a set of 3 (late type) template stars, and used the PPXF (Penalised Pixel Fitting) package from Cappellari & Emsellem (2004) to derive the stellar velocity and velocity dispersion fields. The template stars had been observed with SINFONI, using the same settings as for the M83 data, in order to

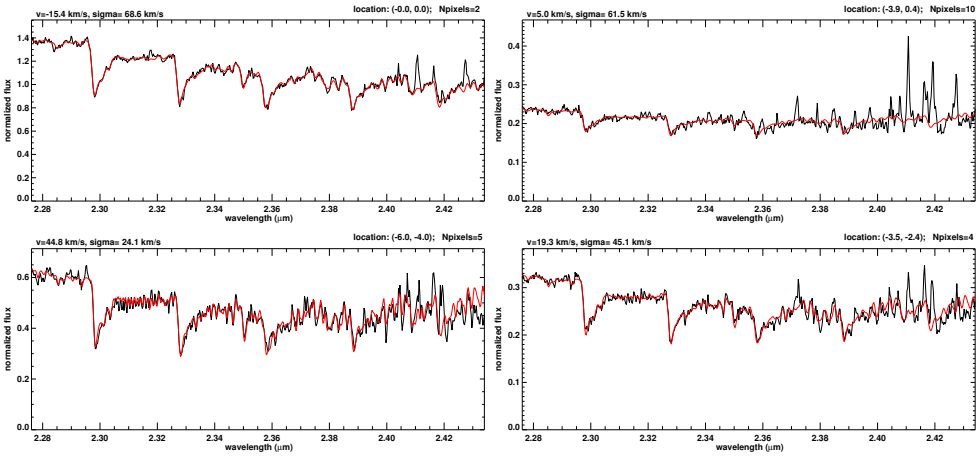

Figure 2.10 – Spectra (black) and PPXF-fits (red) with 3 stellar templates of the spectrum (a) at (0,0), the optical peak A1 (b) at (-3.8,0.2): the starburst location B1, (c) at (-5.9,-4.1): cluster A2 and (d) at (-3.4,-2.5) the centre of outer K-band isophotes. Velocities are relative to the systemic velocity.

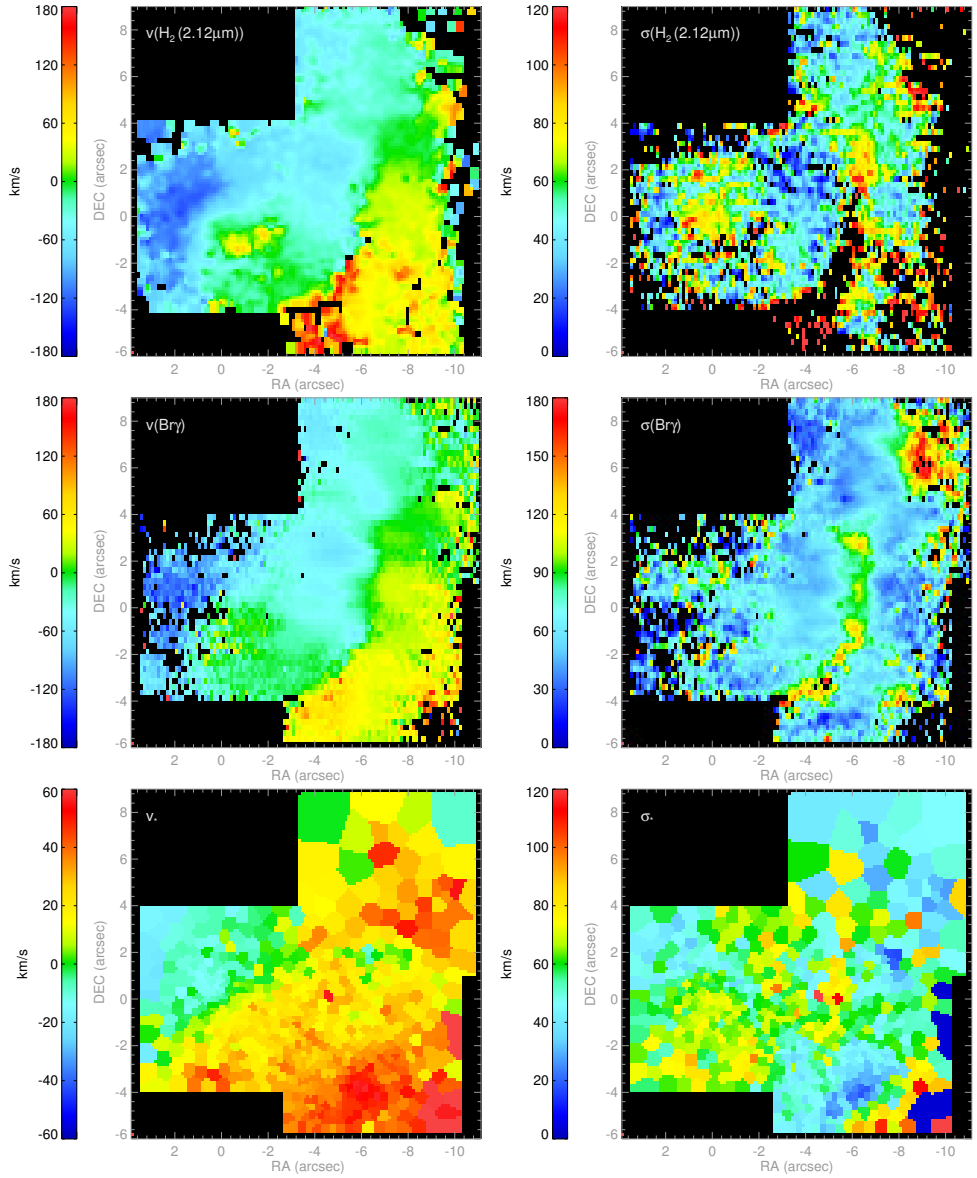

Figure 2.11 – Velocity (left) and velocity dispersion (right). From top to bottom: H_2, Br$\gamma$and stars (CO 2.29μm). In all cases, v_{sys} is set to 520 km/s.

compensate for the effects of instrumental resolution on the fit results. First pixels were combined into bins using a Voronoi tessellation, requiring a S/N ratio of 50 for each bin. Then the combined spectrum of each bin was fitted with the best combination of stars, using a range of velocities and velocity dispersions. The resulting fitted spectra very accurately describe the

observed spectra, in the lower signal regions as well as in the highest continuum peaks, as shown in the sample spectra in Fig. 2.10.

The bottom panel of Fig. 2.11 shows the resulting stellar velocity and velocity dispersion fields. The stellar velocity field (left) looks quite regular, with a high gradient at the optical peak (0,0). The signal in the upper right field is somewhat low, as can be seen from the larger bins, resulting in a somewhat less regular appearance. Overall, the stellar velocity field shows a number of remarkable differences with respect to the gas velocity field, in particular in the region around the optical peak.

Turning now to the stellar velocity dispersion field (Fig. 2.11, lower right), it is remarkable that it does not show a clear peak in the entire region under study. There is a weak enhancement in stellar velocity dispersion at the position of the optical peak ($\sim$75 km/s) but this enhancement extends towards the south as well and does not seem to be centred at the optical peak. We also do not find a clear peak in stellar velocity dispersion west of the optical peak, at the position where the putative dark nucleus of Thatte et al. (2000) would be located. Comparing our data directly with the long-slit spectroscopy of Thatte et al. (2000), we do not confirm the peak in stellar velocity dispersion 2.7″ southwest of the nucleus found by these authors. A very small enhancement in stellar velocity dispersion is found 5″ west of the optical peak, but this position corresponds to one of the main star forming regions and is located outside the position error circle of the putative dark nucleus. In order to demonstrate that our data have more than sufficient S/N for this conclusion to hold, we explicitly include in Fig. 2.10 the central position of the fainter *K*-band isophotes, where the dark nucleus should be located. It can be seen that the observed spectrum is very well fit using the parameters indicated. We therefore firmly discard the scenario of a dark nucleus at the centre of the faint *K*-band isophotes, in agreement with Houghton & Thatte (2008).

2.5.3 Rotating ring structure

Sakamoto et al. (2004) have observed a ring of molecular gas, rotating around a point coincident with the centre of the fainter *K*-band isophotes, offset from the optical peak by about 3″. In principle our kinematic data should allow us to fully determine the parameters of this ring, but in practise this is not possible since our velocity field covers only part of the ring. We therefore fix the centre of the ring at the position found by Sakamoto et al. (2004), and then fit rings of various position angles, inclinations and inner and outer radii to the H_2 velocity field. Of these parameters, the outer ring radius is not constrained at all by our data, and the other parameters are only weakly constrained. A possible geometry with a ring inclination of 55°, major axis position angle of 165°, and inner radius of 120 pc is shown in Fig. 2.12. While we do not insist on the precise values of these parameters (which can unfortunately not be determined accurately due to the partial spatial coverage of the ring), Fig. 2.12 shows a number of striking features, which are common to all acceptable solutions.

1. The ring has a very well-defined inner edge, seen quite clearly by the "jump" in rotation velocities in Fig. 2.12 in the western half of the ring. At positions inside the inner edge, the H_2 velocity field no longer follows the rotating of the ring, but shows a different

kinematic major axis. It is possible that this jump marks the transition between two orbit families in the barred potential of M83, as also suggested by Sakamoto et al. (2004). Indeed, Regan & Teuben (2003) show that nuclear rings in barred potentials are associated with the transition between two orbit families. The ridges of high values in the gas velocity dispersion fields now also have a simple explanation and result from beam smearing where the transition between the two velocity fields (and the two orbit families) occurs. We also note that within the inner edge of the rotating ring, there is little resemblance of the gas and stellar velocity fields, except in the vicinity of the optical peak.

2. A deviation in the velocity field is found at the position of the optical peak, and here the velocity field is dominated by rotation around the optical peak position, as is also seen for the stellar velocity field. Clearly, despite the lack of a stellar velocity dispersion peak, the optical peak represents considerable mass, and dominates the gravitational potential in its immediate surroundings. It is also striking that the optical peak is located quite close to the inner edge of the rotating gas ring.

2.5.4 Nature of the optical peak

Using our kinematic data we can try to constrain the dynamical mass of the optical peak. Taking a slice through the H_2 velocity field with a width of $0.8''$ going through the optical peak at a position angle of 43°(maximising the velocity gradient) reveals a peak line-of-sight rotation velocity of 85 km/s at a radius $1.4''$ (31 pc) from the optical peak. Assuming a spherical mass distribution, the enclosed mass is then $2.6 \cdot 10^7 / \sin^2 i M_\odot$ where i is the orbital inclination of the gas orbiting the optical peak. Unfortunately, i cannot be determined, and it is very uncertain whether its value would be the same as for M83 as a whole (i=24°, Comte 1981). We therefore consider the derived mass a lower limit and note that it could be substantially higher.

With this mass, it is possible that the optical peak could be an evolved superstarcluster, which can have masses of the order to $10^7 M_\odot$, but we consider this unlikely. In the first place, this would require $i \sim 90°$ in order not to exceed observed masses of such objects, and second, such superstarclusters are typically associated with mergers or in dwarf irregular galaxies, and not with grand-design spirals.

The only remaining possibilities are an accreted dwarf galaxy, or an $m = 1$ distortion leading to a displacement of the optical peak from the kinematic nucleus (which would also be the central position of the fainter isophotes). The various arguments are extensively discussed in Houghton & Thatte (2008) and Knapen et al. (2010) and we do not repeat that discussion here. Our results however provide several new elements in this discussion.

1. Our data show that the optical nucleus, while not actively forming stars now, has undergone an episode of star formation in the past, as shown by the presence of several luminous SNRs. This result does not favour any model in particular, but must form part of any scenario constructed to account for the nature of the optical peak.

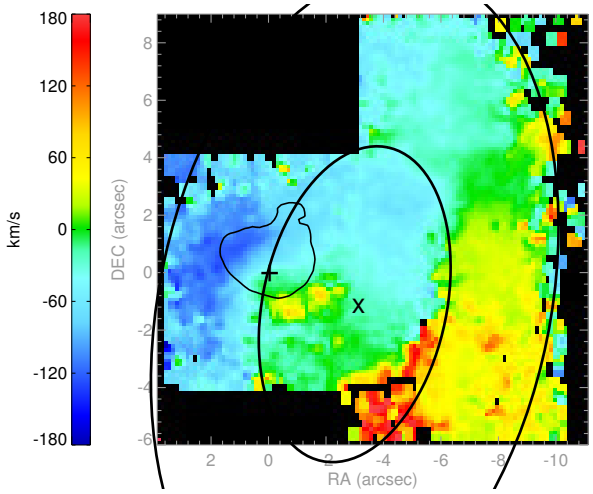

Figure 2.12 – H_2 velocity map. The plus-sign (+) indicates the centre of the optical peak, the cross (x) indicates the location of the centre of *K*-band isophotes. The ellipse indicates the rotating ring, centred on x (inclination 55°, PA of major axis 165°), also observed in CO by Sakamoto et al. (2004).

2. Our data also indicate that the optical peak is located (in projection) quite close to the inner edge of the molecular ring (see Sect. 2.5.3). Obviously, in this complex region we cannot rule out a chance alignment, but if real, this geometry suggests a connection between the ring and the optical peak. It has been suggested that a dynamical relation exists between star clusters and gaseous rings (Van de Ven & Chang 2009) but in that scenario the star clusters would be expected to lie outside the gas ring, contrary to the present situation. An alternative possibility is that the optical nucleus is responsible for the sharp inner edge of the gas ring (Sect. 2.5.3) by accreting gas from its inner edge. Clearly a substantial mass concentration such as the optical peak should affect the structure of the circumnuclear ring if they are physically associated, and indeed Sakamoto et al. (2004) observe an asymmetry in the ring. Note also that the distribution of star formation is asymmetric and concentrated west of the dynamic centre, while the optical nucleus is located east of the dynamical centre. We finally note that the optical peak is displaced blueward in velocity by about 25 km/s from the systemic velocity, as noted by Houghton & Thatte (2008). It is therefore also possible that its motion lies not in the plane of M83, or in that of the circumnuclear molecular ring.

2.6 Summary

The inner 330×330 parsec of M83 is a complex region. Previous studies have shown that the optical peak does not lie at the centre of the fainter isophotes, leading to the suggestion that the galaxy would host a hidden mass concentration at that position. Millimetre observations

revealed that the centre of the fainter isophotes is also the kinematic centre of the galaxy, and forms the centre of a circumnuclear molecular ring.

Our new near-IR integral field spectroscopic data clearly reject the idea of a hidden mass concentration at the kinematic centre, in agreement with Houghton & Thatte (2008) and Knapen et al. (2010). The emerging picture is one where the nuclear region shows a pronounced asymmetry with respect to the kinematic centre. East of the kinematic centre the optical peak is found, which has a mass of at least $2.6 \times 10^7 M_\odot$ and possibly significantly higher. This optical peak may result from an $m = 1$ disturbance of the central region, or may be the remnant of an accreted dwarf galaxy. Whatever its origin, it shows no current star formation, but displays evidence of a recently terminated burst of star formation, given the presence of luminous supernova remnants. The optical peak lies close to the inner edge of the circumnuclear ring, although a chance alignment cannot be ruled out. If this association is real, the optical peak may be responsible for the sharp inner edge of the circumnuclear ring.

Active star formation is concentrated in the region west of the kinematic centre. The young clusters in this region have ages between 5 and 7 Myr, and account for 70% of the total Brγ emission in our dataset (the remaining 30% being diffuse emission). The small age spread suggests a coherent episode of star formation resulting over an approximately 250 pc region. Since the sound travel time over 250 pc would be about 600 Myr (for a 10 km/s sound speed), these results suggest a global instability over a 250 pc region as the trigger for the burst of star formation in this region.

[FeII] emission in our data reveals a large number of compact clumps, quite unlike the distribution of Brγ or H_2 emission. These clumps likely represent individual SNRs, or for the most extended and luminous clumps possibly a small number of SNRs. The integrated [FeII] emission is however dominated by a diffuse component, accounting for 74% of the total [FeII] emission line flux. The large [FeII] 1.257 μm/[PII] 1.188 μm line ratio in the diffuse regions shows that the diffuse [FeII] originates from strong shocks, likely resulting from supernova explosions, just like the compact [FeII] emission.

H_2 rovibrational line emission is found in compact regions associated both with SNRs (where purely thermal H_2 line ratios are found) and with star forming regions (where line ratios reveal UV-pumped fluorescence). Summing over the compact regions, one third of the emission is UV-pumped and two-thirds is shock-excited. However, like for [FeII], the total H_2 emission is dominated by a diffuse component accounting for 75% of the total emission. This diffuse emission is probably thermally excited, given the faintness of the H_2 $v = 2-1$ S(1) line.

In the gas velocity fields, the circumnuclear gas ring observed by Sakamoto et al. (2004) can be recognised. The velocity fields show that this ring has a well defined inner edge. Within the inner edge of the ring a sharp change in kinematic major axis is observed, which may be due to the different orbit families in a barred potential. The gas velocity fields also show rotation around the optical peak in a localised region centred on this peak, and we use this rotation to assign a lower limit to the mass of the optical peak.

Considering the central 330×330 pc of M83 as a whole, its strong asymmetry with respect to the kinematic centre is its most striking feature. This asymmetry manifests itself not only in the eastward displacement of the optical peak but also in the fact that active star

formation is concentrated in the west. It is likely that these two opposite displacements result from a common physical mechanism, and that the large-scale instability giving rise to the synchronised star formation west of the nucleus is related to the same mechanism that resulted in the eastward displacement of the optical peak.

References

Alonso Herrero, A., Rieke, G. H., Rieke, M. J., & Kelly, D. M. 2003, AJ, 125, 1210
Bell, E. F. 2003, ApJ, 586, 794
Black, J. H. & Dalgarno, A. 1976, ApJ, 203, 132
Black, J. H. & Van Dishoeck, E. F. 1987, ApJ, 322, 412
Blietz, M., Cameron, M., Drapatz, S., et al. 1994, ApJ, 421, 92
Bonnet, H., Abuter, R., Baker, A., et al. 2004, The Messenger, 117, 17
Bresolin, F. & Kennicutt, Jr., R. C. 2002, ApJ, 572, 838
Bressan, A., Silva, L., & Granato, G. L. 2002, A&A, 392, 377
Calzetti, D. 1997, AJ, 113, 162
Cappellari, M. & Emsellem, E. 2004, PASP, 116, 138
Carter, B. S. & Meadows, V. S. 1995, MNRAS, 276, 734
Comte, G. 1981, A&AS, 44, 441
Condon, J. J. 1992, ARA&A, 30, 575
Condon, J. J. & Yin, Q. F. 1990, ApJ, 357, 97
Cowan, J. J., Roberts, D. A., & Branch, D. 1994, ApJ, 434, 128
Díaz, R. J., Dottori, H., Aguero, M. P., et al. 2006, ApJ, 652, 1122
Draine, B. T., Roberge, W. G., & Dalgarno, A. 1983, ApJ, 264, 485
Eisenhauer, F., Abuter, R., Bickert, K., et al. 2003, in Presented at the Society of Photo-Optical Instrumentation Engineers (SPIE) Conference, Vol. 4841, Society of Photo-Optical Instrumentation Engineers (SPIE) Conference Series, ed. M. Iye & A. F. M. Moorwood, 1548–1561
Elmegreen, D. M., Chromey, F. R., & Warren, A. R. 1998, AJ, 116, 2834
Fathi, K., Beckman, J. E., Lundgren, A. A., et al. 2008, ApJ, 675, L17
Flower, D. R. & Pineau Des Forêts, G. 2010, MNRAS, 406, 1745
Forbes, D. A. & Ward, M. J. 1993, ApJ, 416, 150
Forbes, D. A., Ward, M. J., Rotaciuc, V., et al. 1993, ApJ, 406, L11
Gallais, P., Rouan, D., Lacombe, F., Tiphene, D., & Vauglin, I. 1991, A&A, 243, 309
Graham, J. R., Wright, G. S., & Longmore, A. J. 1987, ApJ, 313, 847
Graham, J. R., Wright, G. S., & Longmore, A. J. 1990, ApJ, 352, 172
Greenhouse, M. A., Satyapal, S., Woodward, C. E., et al. 1997, ApJ, 476, 105
Harris, J., Calzetti, D., Gallagher, III, J. S., Conselice, C. J., & Smith, D. A. 2001, AJ, 122, 3046
Hollenbach, D. & McKee, C. F. 1989, ApJ, 342, 306
Houghton, R. C. W. & Thatte, N. 2008, MNRAS, 385, 1110
Huang, Z. P., Thuan, T. X., Chevalier, R. A., Condon, J. J., & Yin, Q. F. 1994, ApJ, 424, 114
Hummer, D. G. & Storey, P. J. 1987, MNRAS, 224, 801
Keller, L. D., Jaffe, D. T., Pak, S., Luhman, M. L., & Claver, C. F. 1995, in Revista Mexicana de Astronomia y Astrofisica, vol. 27, Vol. 3, Revista Mexicana de Astronomia y Astrofisica Conference Series, ed. M. Pena & S. Kurtz, 251–+
Knapen, J. H., Sharp, R. G., Ryder, S. D., et al. 2010, MNRAS, 1301
Kroupa, P. & Boily, C. M. 2002, MNRAS, 336, 1188
Labrie, K. & Pritchet, C. J. 2006, ApJS, 166, 188
Lancon, A. & Rocca-Volmerange, B. 1996, New A, 1, 215

Leitherer, C., Schaerer, D., Goldader, J. D., et al. 1999, ApJS, 123, 3
Lumsden, S. L. & Puxley, P. J. 1995, MNRAS, 276, 723
Lumsden, S. L., Puxley, P. J., & Hoare, M. G. 2001, MNRAS, 320, 83
Lumsden, S. L., Puxley, P. J., Hoare, M. G., Moore, T. J. T., & Ridge, N. A. 2003, MNRAS, 340, 799
Maddox, L. A., Cowan, J. J., Kilgard, R. E., et al. 2006, AJ, 132, 310
Martin, P. G. & Whittet, D. C. B. 1990, ApJ, 357, 113
Martins, F., Schaerer, D., & Hillier, D. J. 2005, A&A, 436, 1049
Mast, D., Díaz, R. J., & Agüero, M. P. 2006, AJ, 131, 1394
Mengel, S., Lehnert, M. D., Thatte, N., & Genzel, R. 2005, A&A, 443, 41
Moorwood, A., Finger, G., Biereichel, P., et al. 1992, The Messenger, 69, 61
Morel, T., Doyon, R., & St-Louis, N. 2002, MNRAS, 329, 398
Mouri, H., Kawara, K., & Taniguchi, Y. 2000, ApJ, 528, 186
Neufeld, D. A. & Dalgarno, A. 1987, Phys. Rev. A, 35, 3142
Nussbaumer, H. & Storey, P. J. 1988, A&A, 193, 327
Oliva, E., Marconi, A., Maiolino, R., et al. 2001, A&A, 369, L5
Oliva, E., Moorwood, A. F. M., & Danziger, I. J. 1989, A&A, 214, 307
Oliva, E., Moorwood, A. F. M., & Danziger, I. J. 1990, A&A, 240, 453
Origlia, L., Moorwood, A. F. M., & Oliva, E. 1993, A&A, 280, 536
Origlia, L. & Oliva, E. 2000, A&A, 357, 61
Pak, S., Jaffe, D. T., Stacey, G. J., et al. 2004, ApJ, 609, 692
Pérez-Olea, D. E. & Colina, L. 1995, MNRAS, 277, 857
Regan, M. W. & Teuben, P. 2003, ApJ, 582, 723
Rigby, J. R. & Rieke, G. H. 2004, ApJ, 606, 237
Sakamoto, K., Matsushita, S., Peck, A. B., Wiedner, M. C., & Iono, D. 2004, ApJ, 616, L59
Shields, J. C. 1993, ApJ, 419, 181
Sternberg, A. & Dalgarno, A. 1989, ApJ, 338, 197
Takami, M., Usuda, T., Sugai, H., et al. 2002, ApJ, 566, 910
Thatte, N., Tecza, M., & Genzel, R. 2000, A&A, 364, L47
Thim, F., Tammann, G. A., Saha, A., et al. 2003, ApJ, 590, 256
Turner, J. L. & Ho, P. T. P. 1994, ApJ, 421, 122
Vacca, W. D. 1994, ApJ, 421, 140
Van de Ven, G. & Chang, P. 2009, ApJ, 697, 619
Van der Werf, P. P., Genzel, R., Krabbe, A., et al. 1993, ApJ, 405, 522
Vanzi, L. & Rieke, G. H. 1997, ApJ, 479, 694
Vanzi, L., Rieke, G. H., Martin, C. L., & Shields, J. C. 1996, ApJ, 466, 150
Vázquez, G. A. & Leitherer, C. 2005, ApJ, 621, 695
Walmsley, C. M., Natta, A., Oliva, E., & Testi, L. 2000, A&A, 364, 301
Zaritsky, D., Kennicutt, Jr., R. C., & Huchra, J. P. 1994, ApJ, 420, 87